

The contribution of dissolving star clusters to the population of ultra-faint objects in the outer halo of the Milky Way

Filippo Contenta, Mark Gieles, Eduardo Balbinot, Michelle L. M. Collins

Department of Physics, University of Surrey, Guildford GU2 7XH, UK

December 7, 2021

ABSTRACT

In the last decade, several ultra faint objects (UFOs, $M_V \gtrsim -3.5$) have been discovered in the outer halo of the Milky Way. For some of these objects it is not clear whether they are star clusters or (ultra-faint) dwarf galaxies. In this work we quantify the contribution of star clusters to the population of UFOs. We extrapolated the mass and Galactocentric radius distribution of the globular clusters using a population model, finding that the Milky Way contains about $3.3_{-1.6}^{+7.3}$ star clusters with $M_V \gtrsim -3.5$ and Galactocentric radius ≥ 20 kpc. To understand whether dissolving clusters can appear as UFOs, we run a suite of direct N -body models, varying the orbit, the Galactic potential, the binary fraction and the black hole (BH) natal kick velocities. In the analyses, we consider observational biases such as: luminosity limit, field stars, and line-of-sight projection. We find that star clusters contribute to both the compact and the extended population of UFOs: clusters without BHs appear compact with radii ~ 5 pc, while clusters that retain their BHs after formation have radii $\gtrsim 20$ pc. The properties of the extended clusters are remarkably similar to those of dwarf galaxies: high inferred mass-to-light ratios due to binaries; binary properties mildly affected by dynamical evolution; no observable mass segregation; and flattened stellar mass function. We conclude that the slope of the stellar mass function as a function of Galactocentric radius and the presence/absence of cold streams can discriminate between DM free and DM dominated UFOs.

Key words: methods: numerical, stellar dynamics – star clusters: general

1 INTRODUCTION

The Milky Way halo contains numerous satellite stellar systems with a broad range of luminosities. These stellar systems and their composition contain valuable information about the formation of the Milky Way galaxy (e.g. [Majewski 1993](#); [Tolstoy et al. 2009](#); [Belokurov 2013](#)). Up to a decade ago, there was a clear separation between dwarf galaxies (DGs) and globular clusters (GCs). In a diagram of absolute V -band magnitude (M_V) vs. half-light radius (r_{eff} , see [Fig. 1](#)), GCs (blue squares) and DGs (green circles) with bright luminosities ($M_V \lesssim -3.5$) are separated in size ([Gilmore et al. 2007](#)). On the one hand, DGs are large ($r_{\text{eff}} \gtrsim 30$ pc), whereas GCs are compact ($r_{\text{eff}} \lesssim 10$ pc). In addition, stars within DGs display a range of metallicities ($-3 \lesssim [\text{Fe}/\text{H}] \lesssim -1.5$, [fig. 12 in McConnachie 2012](#)) and their kinematics imply a high mass-to-light ratio, $10 \lesssim M/L_V \lesssim 1000$ ([fig. 11 in McConnachie 2012](#)), which is usually explained by a non-baryonic dark matter component ([Mateo 1998](#); [Gilmore et al. 2007](#); [Walker 2013](#)). Except for a few exceptions, such as ω Cen ([Dickens & Wool-](#)

[ley 1967](#); [Freeman & Rodgers 1975](#); [Butler et al. 1978](#)) and M54 ([Sarajedini & Layden 1995](#)), GCs have no spread in iron abundance ($[\text{Fe}/\text{H}]$), however they do display light-element anomalies ([Gratton et al. 2004](#)) which are not seen in DGs. Moreover, the internal kinematics of GCs can be explained by a single old stellar populations with a ‘normal’ initial stellar mass function (IMF), without the need for dark matter ([McLaughlin & van der Marel 2005](#); [De Marchi et al. 2010](#); [Shanahan & Gieles 2015](#)). Therefore, DGs and GCs were considered to be two totally different classes of stellar systems.

Recently, thanks to the Sloan Digital Sky Survey (SDSS, [York et al. 2000](#)), the Panoramic Survey Telescope And Rapid Response System (Pan-STARRS, [Laevens et al. 2015a](#)), and the Dark Energy Survey (DES, [Bechtol et al. 2015](#); [Koposov et al. 2015](#); [Drlica-Wagner et al. 2015b](#)), several ultra faint objects (UFOs, $M_V \gtrsim -3.5$) have been discovered in the outer halo of the Milky Way (MW). For some MW satellites it is still debated whether they are GCs or ultra-faint DGs ([Willman et al. 2005](#); [Belokurov et al. 2007](#);

Martin et al. 2016). As shown in Fig. 1, at lower luminosities (objects marked in red) the two populations (GCs and DGs) overlap at half-light radii of about 20 to 30 pc (hereafter, we refer to UFO with $r_{\text{eff}} \geq 20$ pc as extended ultra faint objects, eUFO).

Systems in the same magnitude range, but with smaller sizes ($r_{\text{eff}} < 20$ pc), such as Kopusov 1 & 2 (Kopusov et al. 2007), Balbinot 1 (Balbinot et al. 2013), Kim 1 & 2 (Kim & Jerjen 2015; Kim et al. 2015a), are most likely ordinary star clusters, although no spectroscopic follow-up has been done for any of these objects.

Kinematic data excludes the possibility of large amounts of dark matter in some UFOs (e.g. Segue 3, Fadely et al. 2011), but for others, the stellar velocities alone do not allow a conclusive classification (e.g. Segue 1, Belokurov et al. 2007; Simon et al. 2011). In several cases a spread in [Fe/H] is indicative of an extended star formation history and therefore argues for a galaxy classification (Willman & Strader 2012). However, a prolonged star formation history within a dark matter halo does not guarantee that the system contains dark matter at the present day. Tidal stripping and mass segregation could remove the dark matter halo and leave a dark matter free remnant stellar population orbiting the Milky Way (Moore 1996; Mashchenko & Sills 2005a,b; Baumgardt & Mieske 2008).

In the Λ CDM cosmology (Davis et al. 1985; White et al. 1987; Cen et al. 1994; Navarro et al. 1996; Springel et al. 2006; Read 2014), the smallest galaxies are believed to have the highest dark matter density and this makes them promising targets for observing dark matter annihilation signals in γ -rays (e.g. Ackermann et al. 2014). Indeed, the Fermi γ -ray satellite is observing several UFOs (Geringer-Sameth et al. 2015; Drlica-Wagner et al. 2015a), such as the ones that were recently discovered in the Dark Energy Survey data (Bechtol et al. 2015; Koposov et al. 2015). There is an advantage of looking at the UFOs as opposed to the Galactic centre, because they contain fewer known γ -ray sources, such as radio pulsars and low-mass X -ray binaries.

Uniquely establishing whether a UFO contains dark matter is challenging, because only a handful of bright stars are available for spectroscopy and membership determination. In addition, it has been proposed that unbound stars escaping from a dark matter free system could enhance the velocity dispersion and mimic the effect of a dark matter halo (Kroupa 1997). For the UFOs, apart from the kinematic challenge, it is also difficult to determine M_V and r_{eff} , which affects the virial mass estimate because it is proportional to r_{eff} . It is, therefore, not inconceivable that a dark matter free dissolving star cluster appears to have a massive dark matter halo; this was recently proposed for Segue 1 by Dominguez et al. (2016). In this paper, we do not focus our study on a particular object, but we aim to shed light on how many star clusters are expected to contribute to the UFO population.

This paper is organised as follows. In Section 2, we estimate how many faint star clusters (dark matter free objects with $M_V \gtrsim -3.5$ and in the MW-halo) we can expect based on an extrapolation from nearby and bright GCs. In Section 3, we describe the N -body simulations to model star clusters. In Section 4, we discuss the results we obtained considering observational biases, and a summary of our results is presented in Section 5.

2 THE EXPECTED NUMBER AND RADIUS OF FAINT STAR CLUSTER

2.1 Number of faint star clusters

In this section we estimate the number of star clusters that are expected to contribute to the luminosity range of the UFOs by extrapolating from the known GC population.

We use analytic functional forms for the initial distributions of star cluster masses and Galactocentric radii, which we then evolve by a simple mass loss prescription to include the effect of dynamical evolution (two-body relaxation) in the Milky Way potential.

We assume a Schechter function (Schechter 1976) for the clusters initial mass function (hereafter, CIMF; Jordán et al. 2007 for old clusters; and Gieles et al. 2006 and Larsen 2009 for young cluster):

$$\frac{dN}{dM_i} = AM_i^{-\alpha} \exp\left(-\frac{M_i}{M_*}\right). \quad (1)$$

where M_i is the initial mass of star clusters, M_* is the mass where the exponential drop occurs, A is a constant that sets the total mass in clusters and α is the power-law index at low masses $M_i \lesssim M_*$.

Because the Milky Way GCs are old and have lost mass as the result of dynamical evolution, we are interested in the *evolved* mass function (Jordán et al. 2007), which can be expressed in the CIMF by using conservation of number (Fall & Zhang 2001)

$$f(M, R_G) = \frac{dN}{dM} = \frac{dN}{dM_i} \left| \frac{\partial M_i}{\partial M} \right|, \quad (2)$$

where R_G is the Galactocentric radius which enters because the mass evolution depends on the orbit. To proceed, we need an expression for $\partial M_i / \partial M$ that encapsulates the physics of mass loss of GCs. We assume that the dominant mass-loss process is evaporation, which is the result of two-body relaxation in the Galactic tidal field. Baumgardt (2001) showed that for this process, the dissolution time-scale of GCs, t_{dis} , scales with their two-body relaxation timescale, t_{rh} , as $t_{\text{dis}} \propto t_{\text{rh}}^x$, with $x \simeq 3/4$. The mass-loss rate, \dot{M} , can then be written as $\dot{M} = \dot{M}_5(R_G)(M/10^5 M_\odot)^{1-x}$, where $\dot{M}_5(R_G) \simeq 20 M_\odot \text{Myr}^{-1} (\text{kpc}/R_G)$ is the R_G -dependent mass-loss rate found in models of a cluster with a mass of $10^5 M_\odot$ on a circular orbit in an isothermal Galactic potential (Gieles, Heggie & Zhao 2011). From integrating \dot{M} we can find an expression for $M(M_i, \dot{M}_5, \text{Age})$ (Lamers et al. 2005) from which we derive

$$M_i = (M^x + \Delta_x)^{1/x} \quad (3)$$

$$\frac{\partial M_i}{\partial M} = M^{x-1} (M^x + \Delta_x)^{(1-x)/x}, \quad (4)$$

with $\Delta_x = x(1-\epsilon)^{-1}(10^5 M_\odot)^{1-x} \dot{M}_5(\text{Age}/\text{Myr})$, where ϵ is the eccentricity of the orbit. The $(1-\epsilon)^{-1}$ term encapsulates the fact that clusters on eccentric orbits lose mass faster (Baumgardt & Makino 2003; Cai et al. 2016). We adopt $\epsilon = 0.5$, which corresponds to the typical eccentricity of isotropic orbit distribution in a singular isothermal sphere (van den Bosch et al. 1999). Combining equations (2), (3) and (4) we find an expression for the evolved clusters mass

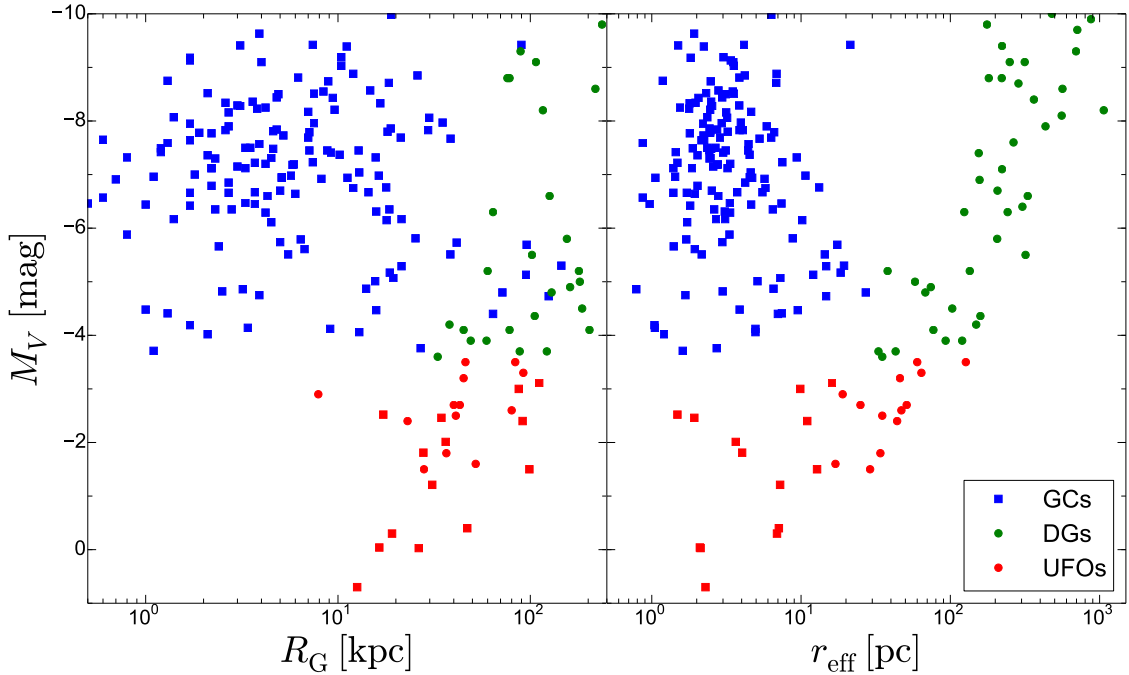


Figure 1. Distribution of Milky Way satellites in the Galactocentric distance-magnitude space (left) and the size-magnitude space (right). GCs are shown as blue squares, DGs are shown as green circles and the faint stellar systems, whose nature has been topic of debate in literature, are in red ($M_V \gtrsim -3.5$). The data on the GCs were taken from [Harris \(2010\)](#), these on the DGs from [McConnachie \(2012\)](#) and the last satellites discovered were included. The recently discovered GCs (blue and red square) are: Segue 3, Muñoz 1, Balbinot 1, Laevens 1/Crater, Laevens 3, Kim 1, Kim 2, Eridanus III, DES 1, Kim 3. While the recently discovered DGs (green and red circle) are: Hydra II, Laevens 2, Pegasus III, Ret II, Eridanus II, Tucana II, Horologium I, Pictoris I, Phoenix II, Draco II, Sagittarius II, Horologium II, Grus II, Tucana III, Columba I, Tucana IV, Reticulum III, Tucana V, Crater 2, Acquarius 2, Pictor II [[Fadely et al. \(2011\)](#); [Muñoz et al. \(2012b\)](#); [Balbinot et al. \(2013\)](#); [Laevens et al. \(2014\)](#); [Belokurov et al. \(2014\)](#); [Paust et al. \(2014\)](#); [Kim & Jerjen \(2015\)](#); [Laevens et al. \(2015a,b\)](#); [Martin et al. \(2015\)](#); [Kim et al. \(2015a,b\)](#); [Bechtol et al. \(2015\)](#); [Koposov et al. \(2015\)](#); [Luque et al. \(2015\)](#); [Drlica-Wagner et al. \(2015b\)](#); [Kim et al. \(2016\)](#); [Torrealba et al. \(2016a,b\)](#); [Drlica-Wagner et al. \(2016\)](#)].

function ([Gieles 2009](#))

$$f(M, R_G) = A \frac{M^{x-1}}{(M^x + \Delta_x)^{\frac{\alpha+x-1}{x}}} \exp\left(-\frac{(M^x + \Delta_x)^{1/x}}{M_*}\right). \quad (5)$$

Because we are interested in finding how many faint star cluster (dark matter free objects with $M_V \gtrsim -3.5$ and $R_G \geq 20$ kpc, hereafter FSC) we expect in the outer halo of the Milky Way, we need to adopt a Galactocentric radius distribution. We decide to use a simple power-law for the initial distribution

$$g(R_G) = \left. \frac{dN}{dR_G} \right|_i = R_G^{2-\beta}, \quad (6)$$

where $-\beta$ is the index of the number density distribution $n(R_G)$, because $g(R_G) = 4\pi R_G^2 n(R_G)$.

The bivariate distribution that we can compare to the data is thus

$$h(M, R_G) = \frac{d^2 N}{dM dR_G} = f(M, R_G) g(R_G), \quad (7)$$

where A in the function $f(M, R_G)$ (equation 5) is a constant that sets the number of clusters after integrating $h(M, R_G)$ over M and R_G . This function can now be used to do a

maximum likelihood fit to find the set of free parameters for which the distribution ($h(M, R_G)$ in our case) becomes most probable:

$$\ln \mathcal{L} = \sum_i \ln \ell_i(p_1, p_2, \dots, p_j) \quad (8)$$

where $\ell_i(p_1, p_2, \dots, p_j)$ is the probability of finding the datum i given the set of parameters p_1, p_2, \dots, p_j . In our case:

$$\ln \mathcal{L} = \sum_{i=1}^{N_{GC}} \ln [h_i(\alpha, \beta, x, M_*)], \quad (9)$$

where $h_i = h(M_i, R_{G_i})$ and N_{GC} is the number of clusters in the sample.

We use the [Harris \(2010\)](#) catalogue of Milky Way globular cluster properties to get M and R_G for each cluster and use $M/L_V = 2$ to convert luminosities to masses. We then use a Monte Carlo Markov Chain (MCMC) method (the affine-invariant ensemble sampler as implemented in the EMCEE code, [Foreman-Mackey et al. 2013](#)) to find the parameters: α , β , x and M_* that give the highest likelihood. We decide to fit equation (7) to the GCs in the M range $3 \times 10^4 < M/M_\odot < 10^7$ and R_G range $0.5 < R_G/\text{kpc} < 20$,

Table 1. Best fit parameters

Parameter	Value	Unit
α	0.452 ± 0.236	
β	3.523 ± 0.128	
x	0.724 ± 0.090	
M_*	4.041 ± 0.964	$10^5 M_\odot$

because this is where we believe the catalogue is complete. The number of selected GCs in that range is $N_{\text{GC}} = 115$. In Tab. 1, we show the results of our best fit parameters. In Fig. 2 we show the resulting best-fit distribution.

We then use the best fit distribution to estimate the number of low-mass GCs at large R_G , where the Harris catalogue is incomplete. With the known parameters of the $h(M, R_G)$ distribution, it is possible to estimate the number of faint star clusters (N_{FSC}) by integrating the distribution over the range where the known UFOs are found ($20 \leq R_G/\text{kpc} \leq 150$; $10^2 \leq M/M_\odot \leq 4.3 \times 10^3$). The lower and upper limit of the mass range correspond to $M_V \simeq 0$ and $M_V \simeq -3.5$, respectively, with our adopted $M/L_V = 2$.

Therefore, the number of faint star clusters is

$$N_{\text{FSC}} = N_{\text{GC}} \int_{10^2 M_\odot}^{4.3 \times 10^3 M_\odot} \int_{20 \text{ kpc}}^{150 \text{ kpc}} h(M, R_G) dR_G dM$$

$$= 3.3_{-1.6}^{+7.3} \quad (10)$$

where the constant A in $h(M, R_G)$ is such that an integration over the range used for the fit results in 1. The quoted value is the median of posterior distribution of N_{FSC} shown in Fig. 3, and the uncertainties correspond to the region containing 68.3% of the points around the median.

In Fig. 2 we show that the extrapolation from the fit to the bright GCs agrees with the number of observed cluster with and without the last observed GC candidates (in orange); however based on this we cannot conclude that a fraction of UFOs need to be galaxies.

2.2 Size estimate of faint stellar systems

The UFOs have sizes up to approximately 100 pc (Fig. 1), but the uncertainties can sometimes be extremely large. Muñoz, Padmanabhan & Geha (2012a) show that it can be challenging to estimate the structural parameters of the ultra-faint DGs within 10% of their true value. For star clusters, it is not known whether it is possible that they appear that large. Here we estimate the maximum radius that a star cluster can have, which corresponds to the situation in which the cluster fills the Roche volume. In that case the half-mass radius (r_h) depends on the strength of the tidal field along the orbit. As described by Hénon (1961), a star cluster evolving in a tidal field, evolves at a constant mean density once it fills the Roche-volume, which means that the ratio between the r_h and the Jacobi radius (r_J) is constant: $r_h/r_J \simeq 0.15$. This fraction is somewhat N -dependent (Alexander & Gieles 2012) and can be as large as $r_h/r_J \simeq 0.4$

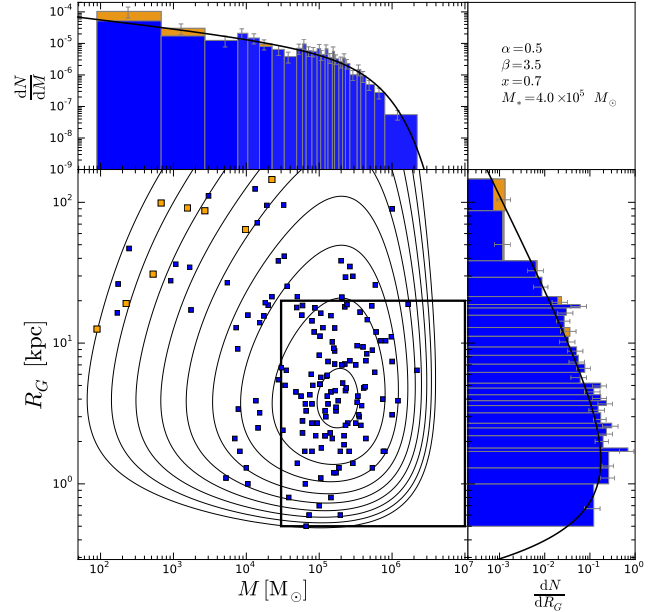


Figure 2. In the bottom left plot we show the Milky Way GCs (blue squares) and the GCs candidates discovered in the last three years (orange squares): Laevens 1/Crater, Laevens 3, Kim 1, Kim 2, Eri III, Balbinot 1, DES 1, Kim 3. The area in the black box is where we compute our fit. In the upper left plot, we have the normalized mass function versus the mass of the GCs, while in the bottom right there is the normalized distribution function versus the Galactocentric distance of the GCs. In blue, the histogram for all the GCs, while the best fit (black line) with α , β , x and M_* as parameters calculated with EMCEE, was found selecting the GCs in this region: $0.5 < R_G/\text{kpc} < 20$ and $3 \times 10^4 < M/M_\odot < 10^7$. The results for the parameters are shown in the upper right plot. In the histograms, the error bars (in grey) are estimated using a Poisson error.

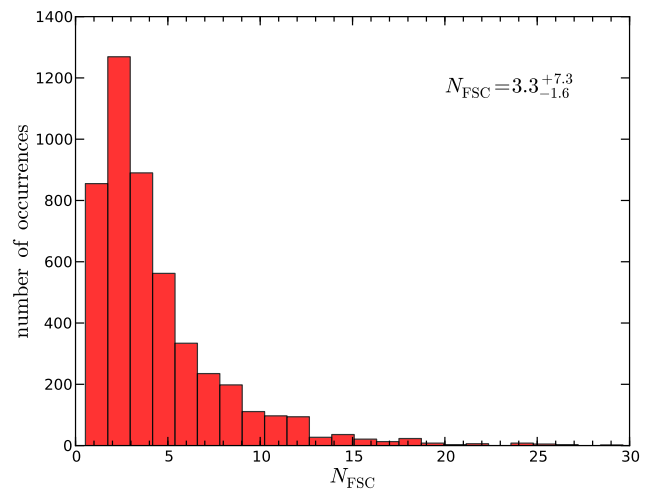


Figure 3. Posterior of the number of faint star clusters (N_{FSC}) marginalised over α , β , x and M_* . The inferred $N_{\text{FSC}} = 3.3_{-1.6}^{+7.3}$.

(Giersz & Heggie 1997) for very small N , i.e. our region of interest. The Jacobi radius is defined in King (1962) as:

$$r_J = \left(\frac{GM}{\Omega^2 - \frac{\partial^2 \phi}{\partial R_G^2}} \right)^{1/3}, \quad (11)$$

where Ω is the angular velocity of the cluster around the Galaxy centre, ϕ is the potential of the Galaxy and G is the gravitational constant. Therefore, using equation (11) and assuming a singular isothermal halo we obtain

$$r_J = \left(\frac{GM}{2\Omega^2} \right)^{1/3}, \quad (12)$$

which is only valid for circular orbit, thus $\Omega = V_C/R_G$.

Therefore, using $r_h/r_J = 0.2$ for a cluster with $M = 500 M_\odot$ at $R_G = 50$ kpc, we find $r_h \simeq 7.6$ pc (with $r_{\text{eff}} \simeq 5.7$ pc, if we assume that mass follows light).

From this we see that the radii of the compact UFOs are consistent with being tidally limited star clusters. However, star clusters in the end of their life have lost most of their low-mass stars, and will therefore have a smaller M , resulting in smaller r_J and hence a smaller r_h . Also, if the cluster is mass segregated, r_{eff} can be smaller than r_h in projection (Hurley 2007). However, observational biases, such as the presence of unbound stars and dark remnants (Peuten et al. 2016) could perhaps inflate r_{eff} with respect to r_h . In the next section we consider the evolution of r_{eff} in numerical models, taking all observational biases into account.

3 NUMERICAL N-BODY SIMULATIONS OF FSCs

3.1 Description of the N -body simulations

In this section we describe the details of the simulations. In order to simulate the evolution of star clusters in a tidal field, we used NBODY6TT (Renaud et al. 2011; Renaud & Gieles 2015b), which is an adaptation of the widely used direct N -body code NBODY6 developed by Nitadori & Aarseth (2012). We use NBODY6TT because we want to consider a Galactic potential that is currently not available in NBODY6. With NBODY6TT it is straightforward to include the tidal field due to an external galactic potential that is a function of position and time. The tidal force is added to the equation of motion of a star in a non-rotating frame by adding the difference in galactic acceleration on the star and the guide centre. The guide centre is a pseudo-particle (initially at the centre of mass of the cluster), and its motion is integrated separately (Aarseth 2003).

We adapt three different Galactic potentials: a static ‘NFW-potential’ (Navarro, Frenk & White 1996), a ‘growing NFW-potential’ (hereafter gNFW, Buist & Helmi 2014), and a three component potential (Paczynski 1990).

34 simulations were performed using the static NFW potential:

$$\phi_{\text{NFW}} = -\frac{GM_0}{R_G} \ln \left(1 + \frac{R_G}{R_0} \right) \quad (13)$$

where the scale mass M_0 is chosen to have a maximum circular velocity $V_C = 210$ km s⁻¹ at $R_C = 30$ kpc, and the scale radius R_0 is 13.9 kpc.

To test the role of the Galactic potential, 8 simulations were performed using the analytical gNFW model of Buist & Helmi (2014):

$$\phi_{\text{gNFW}} = -\frac{GM_s(z)}{R_G} \ln \left(1 + \frac{R_G}{R_s(z)} \right) \quad (14)$$

where the scale mass (M_s) and the scale radius (R_s) evolve with the redshift z as:

$$\begin{aligned} M_s(z) &= M_0 \exp(-0.2z) \\ R_s(z) &= R_0 \exp(-0.1z) \end{aligned}$$

with $M_0 = M_s(z=0)$ and $R_0 = R_s(z=0)$ (same values of eq. 13).

An additional 4 simulations were performed using a three component potential (bulge, disc and halo). We used the analytical model from Paczynski (1990) (hereafter, P90).

Bulge:

$$\phi_b = -\frac{GM_b}{\sqrt{R^2 + (a_b + \sqrt{z^2 + b_b^2})^2}} \quad (15)$$

where: R is the Galactocentric distance in the x - y plane; z is the Galactocentric distance in the z -component; $M_b = 6.15 \times 10^9 M_\odot$; $a_b = 0.0$ kpc; and $b_b = 0.277$ kpc.

Disc:

$$\phi_d = -\frac{GM_d}{\sqrt{R^2 + (a_d + \sqrt{z^2 + b_d^2})^2}} \quad (16)$$

where: $M_d = 4.47 \times 10^{10} M_\odot$, $a_d = 3.7$ kpc, and $b_d = 0.20$ kpc.

Halo:

$$\phi_h = \frac{GM_h}{d} \left[\frac{1}{2} \ln \left(1 + \frac{R_G^2}{d^2} \right) + \frac{d}{R_G} \arctan \frac{R_G}{d} \right] \quad (17)$$

where: $M_h = 3.38 \times 10^{10} M_\odot$ and $d = 6.0$ kpc.

In this paper, we choose different values of the masses for different components with respect to the ones from Paczynski (1990). This difference is due to a rescaling factor, such that the NFW and P90 galaxy models have the same virial mass. We used the ratio between the virial mass of the NFW model ($M_{\text{vir,NFW}} = 1.26 \times 10^{12} M_\odot$) and the virial mass of the original P90 model ($M_{\text{vir,P90}} = 2.29 \times 10^{12} M_\odot$) to rescale the virial mass of the three components in P90. Once the new virial mass of the single components are known it is possible to derive the new M_b , M_d and M_h . The virial mass is the mass of the galaxy within the virial radius, when the mean density of the galaxy is equal to $200\rho_c$, where $\rho_c = 3H_0^2/8\pi G$ is the critical density and $H_0 = 68.0$ km s⁻¹ Mpc⁻¹ is the Hubble constant.

Depending on the orbit and the Galactic potential, stars escape from the cluster as result of two-body relaxation. We therefore need to find the initial N that results in near dissolution (i.e. a few bound stars left) at an age of 12 Gyr.

We used the fast cluster evolution code EMACSS (Alexander et al. 2014) to iteratively find the initial N that satisfies these constraints. We consider both circular and elliptical orbits for the clusters, with eccentricities of $\epsilon = 0$, $\epsilon = 0.25$, 0.5 and 0.75 and with apogalactic distances of 50 kpc, 100 kpc and 150 kpc. In the P90-potential, the apocentre of the clusters were chosen such that the orbits are not planar. Escapers were not removed from the simulations to allow stars to move from the tidal tails back into the region of the cluster because of compression at apocentre. For the initial conditions of all our clusters we used a Plummer model (Plummer 1911) with two different initial densities: clusters that are initially Roche-filling (the stars occupy the total tidal volume), with $r_h/r_J = 0.1$; and clusters that are initially Roche-underfilling (the stars occupy the central region of the tidal volume), where the density within r_h is $\rho_h = 10^4 M_\odot \text{pc}^{-3}$. The stars in the cluster initially follow a Kroupa IMF (Kroupa 2001) between $0.1 M_\odot$ and $100 M_\odot$, and a metallicity of $Z = 0.0008$ (corresponding to $[\text{Fe}/\text{H}] \simeq -1.5$). Moreover, for 7 simulations, we consider the possibility that BHs do not receive a natal kick when they form; as a consequence, we retain 100% of stellar mass black hole initially. While in the other simulations the BHs receive a natal kick velocity which is the same kick velocity given to the neutron stars.

Furthermore, in some models primordial binaries were included, where the binaries components have the same mass. We used the description by Kroupa (1995), where the eccentricities are in thermal distribution with eigenevolution. The distribution of the semi-major axis is either derived from the period distribution, which is initially an uniform log-period distribution or an uniform distribution for the log of the semi-major axis. The properties of the simulations are presented in Table 2.

3.2 Model for the background stars

Typically, observers use simple colour-magnitude cuts to select cluster stars with respect to a fore/background. This method, however, does not completely eliminate the contamination from Milky Way field stars. In order to account for this issue we adopt a synthetic Milky Way stellar population. We used the code TRILEGAL 1.6 (Girardi et al. 2012), which models the Milky Way stellar population for a given region in the sky, we created a map of stars at two positions $(\ell, b) = (158.6, 56.8)$; and $(\ell, b) = (260.98, 70.75)$. The simulated backgrounds are at the positions of the known UFOs, Kopusov 1 (Ko1, Kopusov et al. 2007); and Willman 1 (Will, Willman et al. 2005, 2006, 2011). Ko1 has a small half-light radius ~ 3 pc, while Will1 has a large half-light radius ~ 25 pc, which are extremes in size for this class of objects. Our goal is to see whether a cluster with a different background star density can appear bigger or smaller.

The TRILEGAL sample was created assuming literature values for the reddening (Schlegel et al. 1998). Assuming $R_V = 3.1$ (typical for the Milky Way) and a calibration at infinity, we obtain an extinction of $A_V(\infty) = 0.0418$ for Will1 and $A_V(\infty) = 0.0757$ for Ko1, which is used by TRILEGAL to simulate extinctions which are normally distributed. The scatter on the extinction is also taken from Schlegel et al. (1998) dust maps.

In order to introduce some noise in the reddening correc-

Table 2. N -body simulation properties

Model	R_{apo} [kpc]	ϵ	N	$N_{12 \text{ Gyr}}$
NFW potential				
50e00H	50	0.00	4096	240
50e25H	50	0.25	5000	162
50e50H	50	0.50	6000	184
50e75H	50	0.75	10000	147
50e00L	50	0.00	2048	67
50e25L	50	0.25	3000	44
50e50L	50	0.50	8192	180
50e75L	50	0.75	20000	91
100e00H	100	0.00	2048	212
100e25H	100	0.25	2048	87
100e50H	100	0.50	3000	217
100e75H*	100	0.75	3000	13
100e00L	100	0.00	1024	125
100e25L	100	0.25	1024	71
100e50L	100	0.50	2048	159
100e75L*	100	0.75	8192	29
150e00H	150	0.00	1500	172
150e25H	150	0.25	2048	246
150e50H	150	0.50	1500	44
150e75H	150	0.75	2048	53
150e00L	150	0.00	512	113
150e25L	150	0.25	1024	211
150e50L	150	0.50	1500	183
150e75L	150	0.75	2048	82
50e50M-B1	50	0.50	7200	182
50e50M-B2	50	0.50	7200	227
50e50M	50	0.50	6000	193
50e50H-BH	50	0.50	6000	164
50e50L-BH*	50	0.50	30000	250
50e50L-B2-BH*	50	0.50	30000	0
50e75H-BH	50	0.75	10000	212
50e75L-BH†	50	0.75	32768	32
150e25H-BH	150	0.25	2048	139
150e25L-BH	150	0.25	1200	176
gNFW potential				
50e50H-g	50	0.50	6000	135
50e50L-g	50	0.50	5000	71
50e75H-g	50	0.75	8192	89
50e75L-g*	50	0.75	10000	90
150e25H-g	150	0.25	1500	120
150e25L-g	150	0.25	1024	253
150e75H-g	150	0.75	2048	66
150e75L-g	150	0.75	2048	149
P90 potential				
50e50H-P90	50	0.50	5000	110
50e50L-P90	50	0.50	4096	177
50e75H-P90	50	0.75	10000	166
50e75L-P90*	50	0.75	17000	159

Note. — The capital letter in the model label indicates if the model was, as initial condition, underfilling (high density, H) or Roche-filling (low density, L). In column 4 we show the initial number of stars; column 5 are the number of bound stars at 12 Gyr. The models with the letter M are simulations with a different initial density ($\rho_h = 10^3 M_\odot/\text{pc}^3$), with B1 and B2 contains $\sim 20\%$ of primordial binaries, but different semi-major axis distributions; and with BH retain 100% of BHs initially. In gNFW the value of ϵ is the eccentricity at ~ 12 Gyr. The star (*) and the † denote models for which $r_h/r_J = 0.09$ and $r_h/r_J = 0.06$ respectively, i.e. slightly denser to avoid a high escape rate on a dynamical time.

tion we proceed to correct the TRILEGAL sample assuming a single average value of extinction for the full simulated region. This adds uncertainty to the reddening, which is likely to be the case in real observations.

Furthermore, we assume a photometric error curve ν , with an exponential form, which represent a typical error in mag for each star.

Here the steps to estimate the background number density:

(i) Correction for extinction:

$$\begin{aligned} g' &= g - A_g \\ r' &= r - A_r \end{aligned}$$

where g and r are apparent magnitudes in SDSS filters and g' and r' are the extinction corrected equivalents. For Ko1: $A_g = 0.091$ and $A_r = 0.066$; whereas for Will: $A_g = 0.013$ and $A_r = 0.034$. These values are estimated using [Cardelli et al. \(1989\)](#) and [O'Donnell \(1994\)](#) extinction curve with $R_V = 3.1$.

(ii) Using a photometric error curve:

$$\nu(m, a, b, c) = a + e^{-\frac{m-b}{c}} \quad (18)$$

where m is the observed magnitude corrected for the extinction and (a, b, c) are parameters which depend on the observations; we compute the magnitudes with simulated errors:

$$\begin{aligned} g'' &= g' + \chi \nu(g', a, b, c) \\ r'' &= r' + \chi \nu(r', a, b, c) \end{aligned}$$

where χ is a random number sampled from a Gaussian distribution with mean 0 and variance 1. For Ko1 we use $(a, b, c) = (0.005, 22, 1.2)$; whereas for Will, $(a, b, c) = (0.005, 25, 1.2)$. We choose the value of b to match the limiting magnitude of the observations ([Koposov et al. 2007](#) for Ko1 and [Willman et al. 2006](#) for Will).

We use the above procedure for each star, created with TRILEGAL 1.6, in the field of view of 3 degree, centred in the position of Ko1 and Will.

Finally, we applied the following colour-magnitude cuts: $16 \leq r'' \leq 22$ and $g'' - r'' \leq 1.2$ for Ko1; while $22.6 < r'' < 24.8$ and $0.25 < g'' - r'' < 0.65$ for Will; taking into account only the stars that follow these criteria, we can derive the number of stars per arcsec².

3.3 Maximum likelihood method to fit half-light radii

To estimate the r_{eff} of the simulated clusters, we used a maximum likelihood fit following the procedure outlined in [Martin et al. \(2008\)](#). Having the position of the stars on the plane of the sky, the maximum likelihood fit can find the set of free parameters for which the observations become most probable.

We choose a likelihood (\mathcal{L}) in the following form:

$$\ln \mathcal{L} = \sum \ln (n_P + n_{\text{BG}}) \quad (19)$$

where n_P and n_{BG} are the probabilities of a star belong-

ing to the cluster and background, respectively. We choose n_P to be a 2-D elliptical Plummer profile, given by:

$$n_P = \frac{N_*}{(1-e)\pi a^2} \left(1 + \frac{d^2}{a^2}\right)^{-2} \quad (20)$$

with

$$d^2 = \left[\frac{1}{1-e} (x \cos(\theta) - y \sin(\theta)) \right]^2 + [x \sin(\theta) + y \cos(\theta)]^2 \quad (21)$$

In our likelihood analysis we choose the following parameters: the scale radius (a) which is also the projected half-number radius, the number of stars in the cluster (N_*), the ellipticity¹ (e) and the position angle (θ); while x and y are the positions of the stars on the x - y plane. We can estimate the number of stars in the background N_{BG} , fitting on the parameter N_* , and, knowing the number of stars in our snapshot N_{tot} ($N_{\text{tot}} = N_* + N_{\text{BG}}$). Therefore, knowing the area of our simulated field of view, we can derive n_{BG} , which is considered to be homogeneous across the simulated field-of-views. We use a downhill simplex method ([Nelder & Mead 1965](#)) to find the parameters that maximizes the likelihood. In the following Section we discuss the results of our analysis.

4 RESULTS

In this section we present the results from our analysis, discussing the importance of each observational bias. In this way a comparison between N -body simulations and observational data can tell us something about the underlying properties of the observed objects.

4.1 Example of the evolution of a low- N cluster

To illustrate the evolution of the underlying cluster properties we first present some of the results without considering observational biases. In Fig. 4 we show the properties of the 50e50H model (see Table 2). The upper panel shows the evolution of the absolute V -band magnitude (M_V , see Appendix A for more details on how M_V has been computed) and from this it can be seen that already at approximately 4 Gyr the cluster reaches a luminosity of typical UFOs (see Fig. 1). From then onwards, until the end of the evolution the total luminosity drops by a factor of ~ 15 , and the cluster remains in the luminosity range of UFOs until complete dissolution. From a comparison to the number of bound stars (N_{bound} , middle panel), N_{bound} decreases by a factor of ~ 100 in this period. The slow decrease in luminosity compared to N_{bound} is due to mass segregation and the preferential loss of low-mass stars in the late stages of cluster evolution. This means that our previous estimate of the N_{FSC} in the right mass range is a lower limit (eq. 10), because the N_{FSC} in the correct luminosity range is higher. In the lower panel of Fig. 4, we show the evolution of r_h (bottom blue line) and after about 4 Gyr it levels to a value that is

¹ The ellipticity is defined as $e = 1 - b_0/a_0$ where b_0 and a_0 are the semi-minor and semi-major axis of the ellipse, respectively.

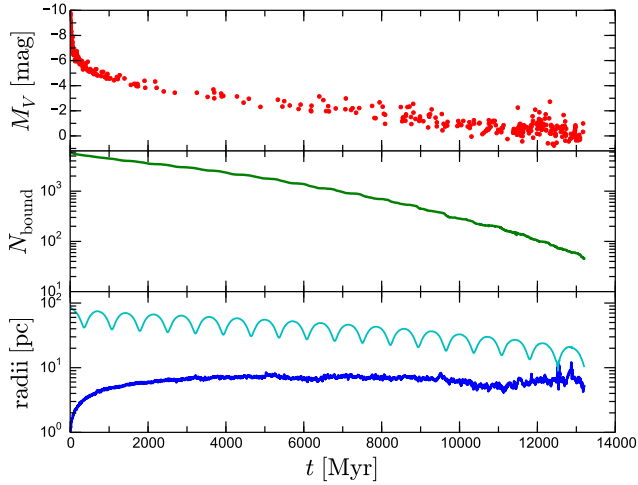


Figure 4. Simulation of a star cluster with initial $N = 6000$, apogalaction at 50 kpc and eccentricity $\epsilon = 0.5$. Top: evolution of the absolute magnitude in the V -band of all the observable particles with $r < 300$ pc. Middle: evolution of the number of bound stars (green line). Bottom: evolution of half-number radius. The blue line is the half-number radius of the bound stars; the cyan line is the tidal radius: in the local minima the cluster is in pericentre, while in the local maxima the cluster is in apocentre.

consistent with filling the Roche volume (see Section 2.2). The top line (cyan) shows the evolution of r_J computed using equation (11) which decreases due to the loss of cluster mass because of escaping stars.

Because some of the above properties, such as N_{bound} , r_h and r_J are not observable, we need to include observational biases in our analyses of the N -body results before we can make a meaningful comparison with the observations. Therefore, in the next section we analyse our data in a similar way as is done for the observational data, as described in Sections 3.2 and 3.3.

4.2 The effect of the background on the size measurements

With the procedure explained in Section 3.2, we include background stars in our simulations. We derive the number density of the background stars (n_{BG}) for two different observed UFOs: Wil1 and Ko1; where $n_{\text{BG}}(\text{Wil1}) < n_{\text{BG}}(\text{Ko1})$. Then, with the cluster in the centre, we add randomly the background stars, uniformly distributed, in an area with a radius of 400 pc, far beyond the tidal radius of a low-mass cluster. Finally, as described in Section 3.3, we compute the best fit Plummer radii, taking only the ‘observable stars’ into account. We consider ‘observable stars’ all the stars with masses greater than $0.5 M_{\odot}$ and which are not dark remnants.

In Fig. 5, we show the evolution of r_{eff} for the model 50e50H. In the last three Gyr, the cluster can reach a large size ($\gtrsim 10$ pc), but only near apocentre, where the largest size ($\gtrsim 20$ pc) is found for the cluster with a low background. In Fig. 6 we show the best fit number density profile for the model 50e50H (see Table 2). The flattening in the external region occurs where the number density of the model roughly

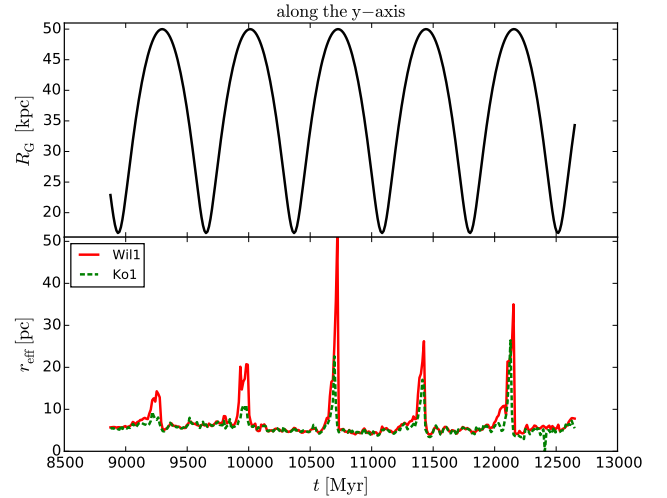


Figure 5. Top: orbit of the cluster. Bottom: Evolution of the half-number radius of the 50e50H model along the y -axis. Half-number radius for a cluster with a Wil1-like background (red line) and a Ko1-like background (dashed green line).

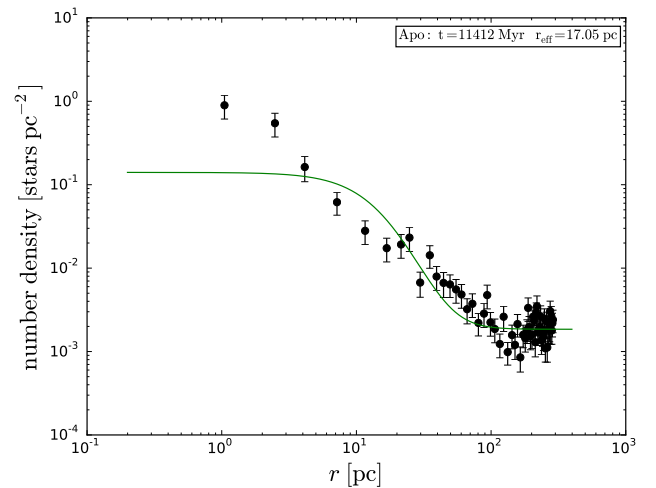


Figure 6. Number density profile of the 50e50H model in apocentre along the y -axis (in this case along the orbit). The green line is the estimated Plummer model using the parameters obtained with the maximum likelihood fit. The Plummer model is not ideal to fit this number density profile because, at $r \sim 25$ pc the bump, caused by the projected positions of the stars in the tails which are close to the centre (in a radius of 400 pc), increases the estimation of the size.

equals to n_{BG} . The simulated cluster is observed along the orbit, near apocentre, where the tails overlap, in projection, with the cluster itself. From this we see that even though r_{eff} is in the correct size range, the Plummer profile does not fit the data properly, because the stars in the tails generate a bump in the number density profile, which is not observed for UFOs (Martin et al. 2008). Whereas, near pericentre, where the tails are elongated, the number density profile is well reproduced by a Plummer model, see Fig. 7.

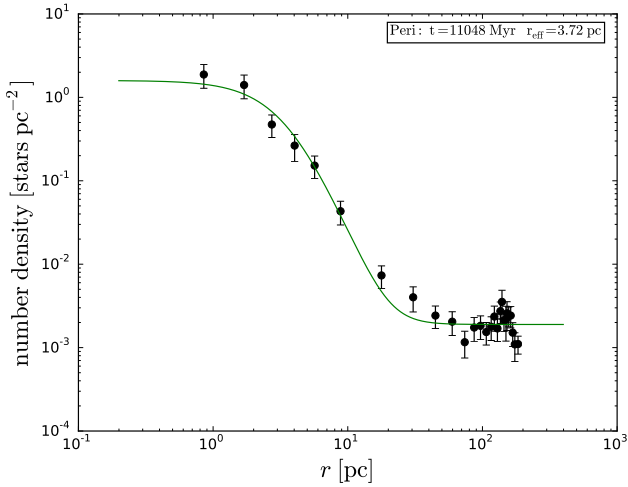


Figure 7. Number density profile of the 50e50H model in pericentre along the y -axis (in this case along the orbit). The green line is the estimated Plummer model using the parameters obtained with the maximum likelihood fit.

4.3 The effect of the line-of-sight on the size measurements

Although we showed that orbital phase can greatly influence the apparent size of a cluster, an additional fact must be considered, which is the dependence on the line-of-sight. To study different lines-of-sight, we translated the N -body coordinates from a non-rotating frame, to a frame in which the cluster is orbiting in the x - y plane with positive angular momentum centred on the Galaxy and with the x -axis increasing towards the cluster. As shown in Fig. 5, along the y -axis near apocentre the cluster reaches $r_{\text{eff}} \sim 20$ pc, while when viewed along the x -axis and z -axis, Fig. 8, we do not see any variations in the r_{eff} measurements linked to the orbital motion. As a consequence, these star clusters appear as eUFO only when observed along the y -axis and when they are near apocentre. For all the simulations, the results for the x and z directions are identical, therefore, in the following figures we will show only one of them.

Because in our chosen reference frame, the y -axis is not along the orbit in between pericentre and apocentre, we also considered the cluster’s properties along the orbit at those positions, to see whether the projected tails can influence the measured cluster’s size. Near apocentre and pericentre we expect to obtain the same results as when we observe the cluster along the y -axis, because in pericentre the two lines-of-sight overlap. For the entire evolution of the cluster, we found that the estimation of the size along the y -axis and along the orbit are comparable.

The y -axis is the only line-of-sight along which we can observe clusters with a large size, however it is also the least probable one; because these objects are in the halo of the Milky Way ($R_G \gtrsim 20$ pc). Therefore, unless they have their pericentre within the solar circle, it is impossible to observe them along the orbit.

To quantify the probability to observe an eUFO, we estimated the fraction of orbit (f_t) in which a cluster appears extended. Therefore, f_t is the ratio between the time when a

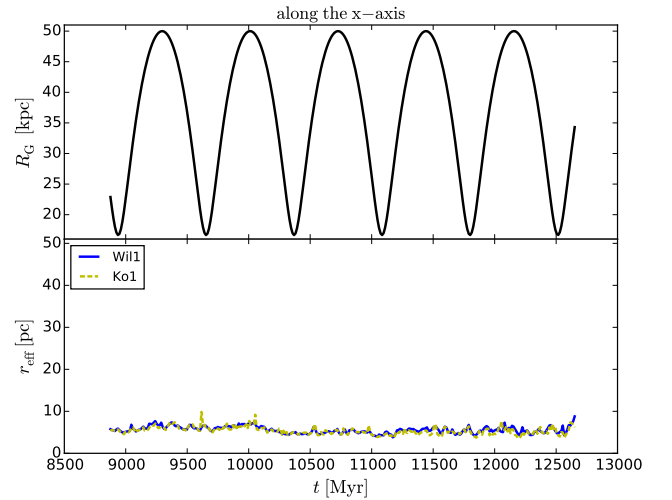


Figure 8. Top: orbit of the cluster. Bottom: Evolution of the half-number radius of the 50e50H model along the x -axis. As in Fig. 5, half-number radius for a cluster with a Wil1-like background (blue line) and a Ko1-like background (dashed yellow line).

cluster appears extended and its orbital period. For the simulation 50e50H along the y -axis $f_t \sim 0.08$, but if we take into account the fact that along the other lines-of-sight $f_t = 0$ then the probability to observe the cluster is $< 1\%$.

4.4 The effect of the initial cluster density on the size measurement

An additional parameter to take into account is the initial cluster density. As shown in Table 2, we divide our simulations in high density (H) and low density (L) clusters. The low density clusters fill the Roche-volume initially while the high density clusters are initially Roche-underfilling.

Hénon (1961) showed that a cluster, once it has filled its Roche-volume, evolves with a constant ratio of r_h over r_j (Sec. 2.2). Therefore, we expect that the evolutions of r_{eff} of the clusters on the same orbit but with different initial densities are similar in the final stage of evolution.

We find that this is indeed the case for most of our models (Fig. 9). However, we find that there is a difference in the evolution of r_{eff} depending on the initial density for three of our orbits: $R_G = 50$ kpc and $\epsilon = 0.75$; $R_G = 50$ kpc and $\epsilon = 0.50$; $R_G = 100$ kpc and $\epsilon = 0.75$.

In Fig. 10 we show an example of the r_{eff} evolution for two models on the same orbit with different initial densities and it can be seen that r_{eff} of the low-density cluster always lays above r_{eff} of the high-density cluster. We interpret this difference as being due to the slow removal of stars in the early evolution of the clusters with low densities that stay near the cluster and can enhance r_{eff} at later stage. The high density cluster loses stars in all directions with higher velocity in the initial phases, and these stars are then too far to affect the r_{eff} measurement. Furthermore, we observe a greater variation of r_{eff} due to the orbital motion, visible in all the lines-of-sight for these three orbits, in the simulations with a low initial density. Whereas the clusters

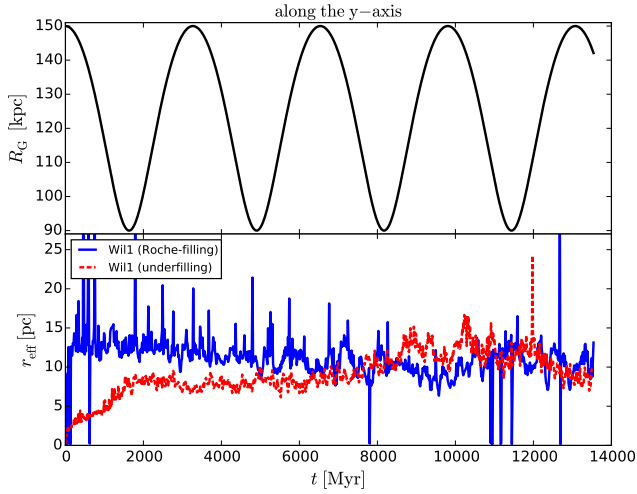


Figure 9. Top: orbit of the cluster. Bottom: Evolution of the half-number radius of the 150e25H (dashed red line) and 150e25L (blue line) models along the y -axis.

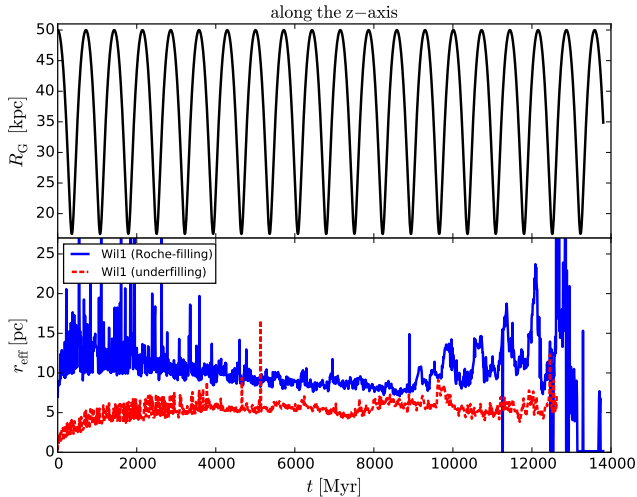


Figure 10. Top: orbit of the cluster. Bottom: Evolution of the half-number radius of 50e50H (dashed red line) and 50e50L (blue line) models along the z -axis (same results for the x -axis). Both the models have a Wil1-like background.

with a high initial density appear larger only along the y -axis. Therefore, to observe an extended cluster along all the lines-of-sight, this has to initially have a low density. For these simulations f_t can be as high as ~ 0.54 , this estimate changes for different orbits and whether the cluster is close to dissolution.

4.5 The effect of cluster's orbit on the size measurement

To understand the relation between the orbit of a cluster and its r_{eff} , we illustrate in Fig. 11 the pericentre (R_p) and the apocentre (R_a) of each orbit considered in this paper in a static NFW potential (Table 2). Therefore, each point

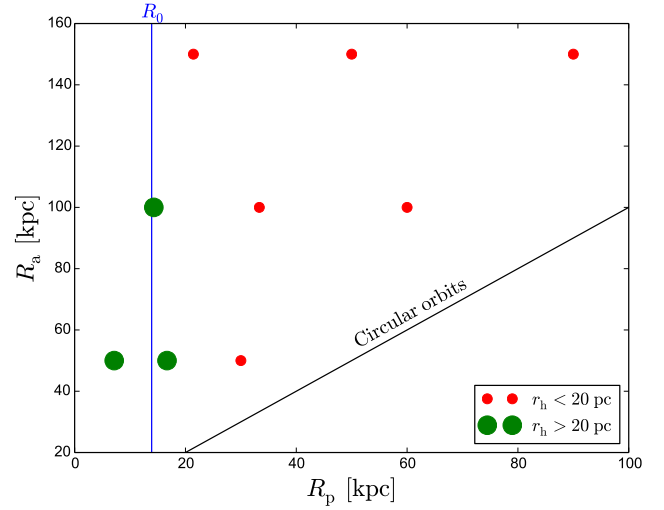


Figure 11. Effect of cluster orbits. The green dots show when we observe a cluster larger than 20 pc in any line-of-sight, while the red dots show orbits of clusters that are always smaller than 20 pc. R_0 is the scale radius of the NFW potential. As shown, the simulations that have their pericentre close or within the scale radius reach a larger size. For initially Roche-filling clusters and close to dissolution, f_t can be as high as ~ 0.19 , ~ 0.45 and ~ 0.54 , for the models 50e50L, 50e75L and 100e75L, respectively.

represents an orbit. The colours mark whether the size of a cluster can appear larger than 20 pc (in green) or not (in red), due to the variation in the size evolution, as shown in Fig. 5.

Surprising, in Fig. 11 the three green dots represent the three orbits mentioned in the previous section (where r_{eff} evolution for different initial density never overlap). We find that these three orbits have their R_p either close or within the scale radius (R_0 , blue vertical line) of the Galactic potential, where the slope of the NFW density profile changes. A variation of the Galactic density profile implies a different evaporation mass loss of the cluster during its pericentre passages. In these orbits, the stars that escape at R_p are easily coming back close to the cluster, so that they can inflate the size measurement, especially when the cluster is initially Roche-filling.

Among the simulations with a pericentre close to R_0 , the simulations 150e75H and 150e75L which have $R_p = 21.4$ kpc do not appear larger. Therefore, we assume that all the clusters with $R_p < 20$ kpc appear larger. Considering only orbits with pericentre within 20 kpc and the f_t in the previous Section, the probability to observe an eUFO, that was initially Roche-filling, can be as high as $\sim 30\%$.

4.6 The effect of different potentials

To understand the role of the Galactic potential, we run additional simulations using different MW-like potentials; gNFW and P90.

In the previous section, we conclude that the scale radius of the Galactic potential has an important role to discern between star clusters and extended star clusters.

In a static potential, clusters orbiting around a galaxy

have their pericentre fixed in time (dynamical friction is negligible and has not been taken into account), while in a growing potential, clusters that have their pericentre within the scale radius at 12 Gyr could have their pericentre beyond the scale radius initially.

Results from our simulations show that a gNFW potential (see Sec. 3.1) does not change the evolution of star clusters, because the stars that inflate the size of a cluster in the last few Gyr are the ones that have escaped recently from the cluster. The properties of the simulations are presented in Table 2.

Renaud & Gieles (2015a) showed that cluster evolution does not change in a gNFW potential also for satellites that have $R_a \leq 50$ kpc. In our case, we tested clusters with $R_a \geq 50$ kpc, because, as described in Buist & Helmi (2014) galaxies form inside out (Helmi et al. 2003; Wang et al. 2011). Which means that the mass of the MW is growing in shells by smooth accretion; therefore, the objects in the halo should be more affected by the growth of the DM potential.

After testing a growing halo potential, we studied the evolution of clusters in a potential which includes a bulge, disc and halo component. The disc could influence clusters which have their pericentre close to the Galactic centre. Moreover, with a multi-component potential we can have non planar orbits, increasing the probability to observe a cluster from different lines-of-sight.

To assess the effects of a multi-component potential, we run four simulations using a static potential for the bulge, the disc and the halo, following the analytical model from P90 (see Sec. 3.1). The properties of the simulations are presented in Table 2.

Even in this case the evolution of the observed size is similar to the simulations with a NFW potential. Therefore, we conclude that, with our initial conditions, the passage of a cluster through the disc does not enhance the size of the cluster, because the scale parameter of the disc ($a_d = 3.7$ kpc) is roughly half of the minimum pericentre distance ($R_p = 7.14$ kpc).

4.7 The effect of stellar mass black holes retained in the cluster

There are no observational constraints on black hole (BH) natal kicks, while there are on neutron star natal kicks, mainly thanks to radio pulsars. For this reason, it is not clear whether the BHs natal kick should be similar (Repetto et al. 2012) or smaller than the neutron stars natal kick (Fryer et al. 2012). Likely, with the discovery of new gravitational waves, further constraints will be set on the BHs natal kick velocity (Abbott et al. 2016).

It has been shown by Merritt et al. (2004); Mackey et al. (2007, 2008); Lützgendorf et al. (2013) and Peuten et al. (2016) that a higher fraction of dark remnants in a cluster can change its observed properties. Moreover, BH candidates have been observed in several GCs (Strader et al. 2012; Chomiuk et al. 2013); as a consequence, we consider the possibility that BHs do not receive a kick when they form and for these models we retain 100% of stellar mass BHs initially. The properties of the simulations are in Table 2 and for the Galactic potential we assumed a NFW potential (eq. 13).

In Fig. 12 we show the evolution of r_{eff} for the model

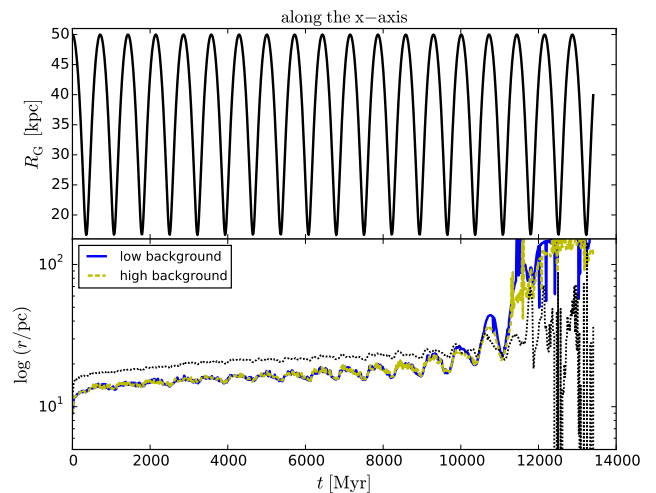


Figure 12. In the lower plot, evolution of the half-number radius of the 50e50L-BH model along the x -axis. Half-number radius for a cluster with a Will-like background (blue line) and a Ko1-like background (dashed yellow line), 3D half-mass radius (dotted black line). In the upper plot the black line shows the orbit of the cluster.

50e50L-BH that started with a low initial density. The clusters appear extended ($r_{\text{eff}} \gtrsim 20$ pc) for almost the entire evolution (after roughly 9 Gyr), independent of the projection axis (similar results for other lines-of-sight) and orbital phase. Indeed, the projection effect of the tails are not affecting the fitting results as in Fig. 6. Therefore, unlike the models that do not retain BHs, these clusters can be observed as eUFO ($f_t = 1$).

In Fig. 13, the evolution of the fraction of BHs inside the cluster (within the tidal radius) shows how fast the BH population escape from the cluster. Breen & Hoggie (2013a,b) showed that the escape rate of stellar BHs depend on their half-mass relaxation time.

For clusters with high initial density, for example in the simulation 50e50H-BH, because the short initial half-mass relaxation time ($t_{\text{rh},0}$), all the BHs are dynamically ejected in few Gyr; indeed, the results are similar to the simulation 50e50H where only few percent of BHs are retained in the cluster initially. Whereas, the low density clusters, which have a $t_{\text{rh},0}$ of $\sim 2 - 3$ Gyr, as shown in Fig. 13 they retain the BHs up to the dissolution of the cluster. These low density clusters do not appear mass segregated (Peuten et al. 2016). The effect of stellar mass BHs retained in low density clusters is remarkable, because these clusters can appear as large as an eUFO for the last Gyr (not only near apocentre) and along all the lines-of-sight. However, in the absence of kinematics, it is challenging to determine whether these objects are DM free or dominated, because they do not appear mass segregated. Regarding their morphology, if we observe them along the x -axis (the most probable line-of-sight), we do not see the typical ‘S’ shape of a star cluster, because the Lagrangian points (L1 and L2) overlap with the centre of the cluster.

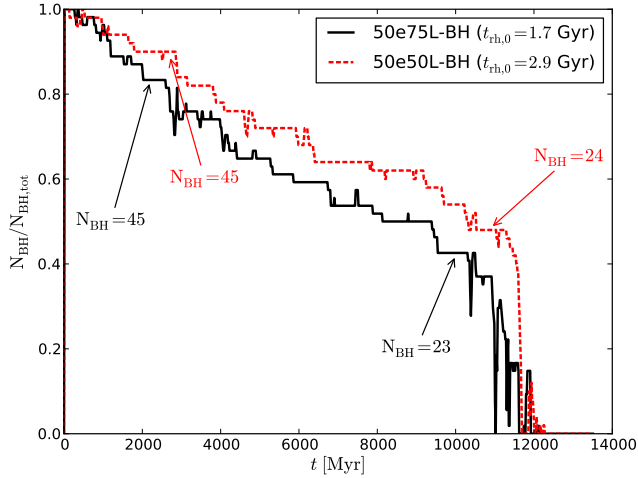


Figure 13. Evolution of the fraction of BHs (normalized to the maximum value) for the models 50e50L-BH (dashed red line) and 50e75L-BH (black line), within the tidal radius of the clusters

4.8 Mass function

In this section we want to study the mass function (MF) of collisional system with large $t_{\text{rh},0}$ ($\sim 2 - 3$ Gyr), where the BHs are retained.

In Fig. 14, we plot the MF of the N -body model 50e50L-BH, for all the stars without the dark remnants (blue line) and for the white dwarfs (WDs, orange line). Then we compare the MF of our model with a single stellar population (SSP) model. For the SSP model we assumed a Kroupa IMF (Kroupa 2001) between $0.1 M_{\odot}$ and $100 M_{\odot}$, and a metallicity of $Z = 0.0008$ (corresponding to $[\text{Fe}/\text{H}] \simeq -1.5$). We evolve the SSP model, up to 11 Gyr, with the single-star evolution (SSE, Hurley et al. 2000) code, which is the same evolutionary tool available in NBODY6. The MF of the SSP model is in dashed cyan line for all the stars except the dark remnants, and in dashed magenta line we plot the WDs. To compare these models we scaled the SSP MF to the N -body MF, such that the number of stars in the last bin of the observable stars ($0.79 < m/M_{\odot} < 0.87$) is the same for SSP and N -body model. From this comparison (Fig. 14), we can say that in collisional systems, where dynamical interactions between stars are important, the MF is flattened. Because ultra-faint dwarf galaxies appear to have similar MF slopes (~ -1.3 in the range $0.5 - 0.77 M_{\odot}$, Geha et al. 2013), the flattened MF as a result of dynamical evolution can not be used to discern between extended star clusters and DGs for an individual object. However, for star clusters we do not expect a relation between the MF slope and the metallicity (as found for DGs), but we do expect the slope to be flatter at smaller R_G (e.g. Vesperini & Heggie 1997). Hence the MF slope might be useful for addressing the nature of UFOs by considering the MF slope as a function of R_G and $[\text{Fe}/\text{H}]$, simultaneously.

As shown in Fig. 14, the model 50e50L-BH shows a large fraction of WD. To estimate how many WD are present in the models with respect to the observable stars, we estimate the number of WD (N_{WD}) between the first bin of the WD and the last bin of the observable stars, and the

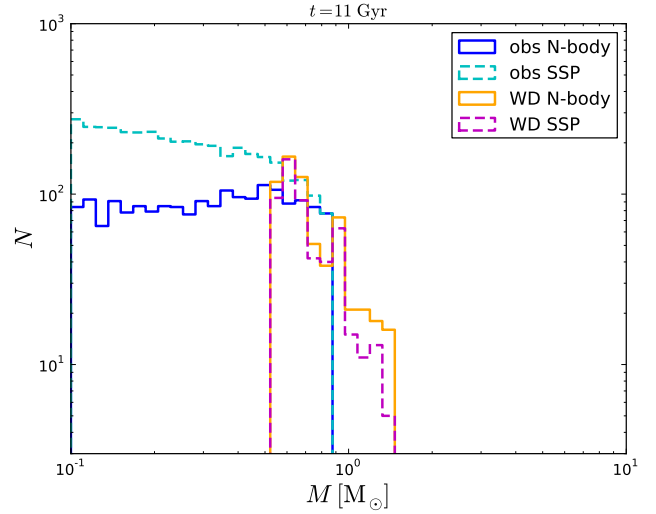


Figure 14. Stellar mass function for the model 50e50L-BH and for a stellar population with the same IMF and age (SSP), but that has undergone no dynamical evolution, after 11 Gyr.

same for the number of observable stars (N_*). Therefore, for $0.52 < m/M_{\odot} < 0.87$, $N_{\text{WD}}/N_* = 0.76$ for the SSP model and $N_{\text{WD}}/N_* = 1.12$ for the N -body model. Goldsbury et al. (2012) and Heyl et al. (2015) show that, in the UV, the young WD are among the brightest stars in the cluster, which means that for FSC the WD population can potentially be observed. However, in a low- N system such as a UFO, the number of young WD is small. For example, with HST in the F225W band, for the model 50e50L-BH at 11 Gyr we expect to be able to observe only 4 out of 499 WD.

4.9 Velocity dispersion

To establish the dynamical mass of a system we need r_{eff} and the velocity dispersion, σ . Despite the fact that it is challenging to determine σ for most UFOs, because of their distance and the limited number of bright stars, for some of them the velocity dispersion has been measured. For example, Will has $\sigma \sim 0 \text{ km s}^{-1}$ within r_{eff} (Willman et al. 2011), which is consistent with a star cluster scenario; whereas Segue 1 has $\sigma \sim 3.7^2 \text{ km s}^{-1}$ within $\sim 3 \times r_{\text{eff}}$ with a V -band mass-to-light ratio of $3400 M_{\odot}/L_{\odot}$ (Simon et al. 2011), which lead to the conclusion that Segue 1 is a dark matter dominated object. We analysed our simulations keeping in mind the observational biases discussed previously in this paper, and studied whether it is possible to infer a high velocity dispersion in a dark matter free object. We assumed that with a velocity measurement, member stars and background stars can be separated, and we therefore ignore the effect of background stars on the σ measurements. Moreover, we studied the kinematics of the FSCs, to see whether the orbital motion of the cluster could leave some features in the velocity dispersion profile like in r_{eff} along the orbit near apocentre (Fig. 5), as this has been the proposed scenario for the high

² Giant stars show a lower velocity dispersion, $\sigma \sim 2_{-1.7}^{+3.1} \text{ km s}^{-1}$.

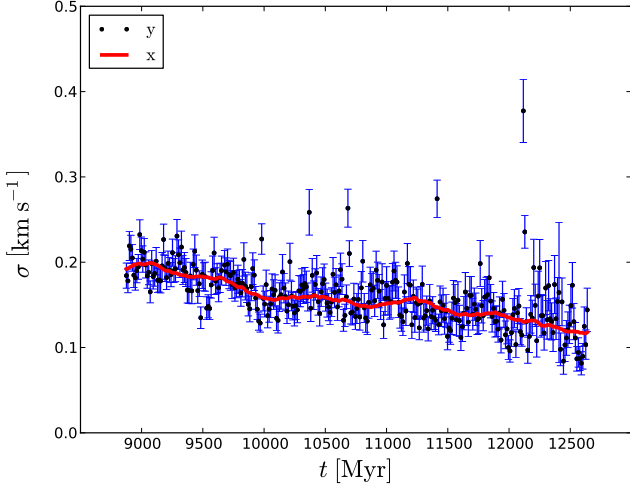


Figure 15. Evolution of the velocity dispersion of the model 50e50H along the x -axis (red line) and along the y -axis (black dot).

σ of dwarf spheroidal galaxies (Kroupa 1997 but see Mateo 1997 and Olszewski 1998). To compute the σ , we are taking all the observable stars into account (see Sec. 4.2), within r_{eff} , along a line-of-sight, as a function of time.

Therefore, the velocity dispersion σ_j is defined as:

$$\sigma_j^2 = \frac{1}{(N_h - 1)} \sum_i^{N_h} (v_{j,i} - \bar{v}_j)^2 \quad (22)$$

where j is a chosen line-of-sight, N_h is the number of stars within the projected half-number radius, $v_{j,i}$ is the velocity of the i -th star in the line-of-sight and \bar{v}_j is the mean line-of-sight velocity; and we estimate the variance for each velocity dispersion as (Pryor & Meylan 1993)

$$\Delta\sigma_j^2 = \frac{\sigma_j^2}{2N_h}. \quad (23)$$

In Fig. 15, we show the velocity dispersion along the x -axis (red line) and along the y -axis (black dots). The other line-of-sight, z , is not shown because it has the same trend and values of the x -axis. As shown, there are only features due to the orbital motion along the y -axis when the cluster is near apocentre. The cause of increase is similar to what we found for the enhancement of r_{eff} along the y -axis, namely an increased number of unbound stars projected within r_{eff} . Nevertheless, as shown in the Fig. 15, this rise happens only for a brief moment with respect to the orbital period, near apocentre. Because of this, and the fact that it is impossible to view a system exactly along its orbit when it is in apocentre (if the apocentre distance is further away than the solar radius), this effect is not expected to play an important role in inflating the velocity dispersion, at least not in the cases studied here. Therefore, any observation of the velocity dispersion of a FSC without binaries in the outer halo should find a value that is consistent with the virial mass of the stars and stellar remnants (i.e. a few 100 m s^{-1}).

4.10 Binaries

Around one-third of the stars in the solar neighbourhood are in binaries or multiple systems (Lada 2006) and UFOs may have a higher fraction of binaries (e. g. Simon et al. 2011; Martinez et al. 2011). Previous studies show that binaries play an important role in the cluster’s evolution (Heggie & Hut 2003; Ivanova et al. 2005; Hurley et al. 2007). NBODY6 includes a prescription for both single star and binary star evolution (Hurley et al. 2000, 2002) and allows us to study these effects combined with their dynamical influence on the evolution of the cluster. In this Section we focus our efforts in understanding and quantifying the effect of primordial binaries on the velocity dispersion, performing three simulations with $\sim 20\%$ of primordial binaries (50e50M-B1, 50e50M-B2 and 50e50L-B2-BH).

We report in Table 2 the three runs. For 50e50M-B1 and 50e50M-B2 we have the same initial conditions as for the other clusters, except that the initial density is lower with respect to the high density simulations. In these two simulations, as for 50e50M, we have $\rho_h = 10^3 \text{ M}_\odot \text{ pc}^{-3}$ with an apogalacticon of 50 kpc and eccentricity of 0.50.

In Fig. 16 we show the evolution of r_{eff} for the model with binaries (50e50M-B1) and without (50e50M). The values for r_{eff} between the two simulation are similar therefore we can conclude that primordial binaries do not inflate r_{eff} . Previous studies (Giersz & Heggie 2011) showed that the evolution of r_h is insensitive to the binary fraction.

For the analyses we treat stars in binary systems in the same way as the single stars, i.e. if their luminosity is above the detection limit, we include them in the analyses of σ . This means that there is an additional contribution to σ due to the orbital motion of the binary members. As is often done in observations, we apply a σ -clipping technique iteratively, removing all the stars with velocities larger/smaller than 3σ from the mean, until the value of the σ does converge (Yahil & Vidal 1977).

In Fig. 17 we show the evolution of the velocity dispersion for the 50e50L-B2-BH model; which dissolve after 11 Gyr. The increase in the observed σ due to binaries is small (green line) with respect to the same model without primordial binaries (black line). Towards the end of the cluster evolution we observe an increase in σ associated with the increased number of binary systems, this increase is due to preferential loss of low-mass single stars (Ivanova et al. 2005; Hurley et al. 2007). However, if the σ -clipping technique it is not taken into account (red line in Fig. 17), for example for a low number of observable stars, then the velocity dispersion is roughly 1 km s^{-1} . During the evolution of the cluster, the binary properties hardly change because the model has a large $t_{\text{rh},0}$ (see Sec. 4.7), while there typically only a few dynamically formed binaries (which have a short orbital period). Because the dynamical velocity dispersion is low ($\sim 0.1 \text{ km s}^{-1}$), binaries with orbital velocities of $\sim 0.5 \text{ km s}^{-1}$ are significantly affecting the inferred velocity dispersion. For a primary of 0.7 M_\odot and a secondary 0.4 M_\odot this corresponds to a period of $\sim 1000 \text{ yr}$, making it very challenging to detect these binaries in repeat observations. Because the binary properties do not evolve much, the only way of taking binaries into account would be to make an assumption about the binary properties and include this in

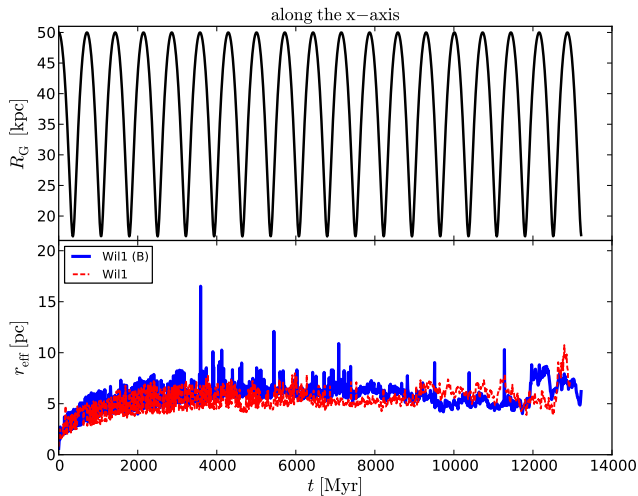


Figure 16. Evolution of r_{eff} with (blue line) and without (dashed red line) primordial binaries along the x -axis. In blue r_{eff} of 50e50M-B1 and in red r_{eff} of 50e50M. The black line shows the radial orbit of the cluster.

the modelling (e.g. [Martinez et al. 2011](#); [Cottaar & Hénaux-Brunet 2014](#)).

Assuming that the model 50e50L-B2-BH at 10 Gyr is in dynamical equilibrium, with the formula by [Walker et al. \(2009\)](#) and [Wolf et al. \(2010\)](#) we can estimate its dynamical mass within the half-light radius of the system:

$$M_{1/2} = \frac{4}{G} \sigma^2 r_{\text{eff}}. \quad (24)$$

For example, for $\sigma \simeq 1 \text{ km s}^{-1}$ and $r_{\text{eff}} \simeq 30 \text{ pc}$, $M_{1/2} \simeq 2.8 \times 10^4 M_{\odot}$. From the simulation we can estimate the half-light luminosity $L_V \simeq 700 L_{\odot}$, therefore the $M/L_V \simeq 40 M_{\odot}/L_{\odot}$, which is consistent with a DM-dominated object interpretation. While if we consider the 3σ -clipping, $\sigma \simeq 0.4 \text{ km s}^{-1}$ then $M_{1/2} \simeq 4.5 \times 10^3 M_{\odot}$ and $M/L_V \simeq 6 M_{\odot}/L_{\odot}$. Because r_{eff} and σ change with time, in the cluster lifetime we have different estimates of the M/L_V , which can be as high as $100 M_{\odot}/L_{\odot}$.

Our estimation can be interpreted as a lower limit, because we do not have background stars that can contaminate the measurements of the velocity dispersion.

5 CONCLUSIONS

In this study we present N -body simulations of the evolution of faint star clusters (FSCs) using NBODY6TT, which is an adaptation of the direct N -body code NBODY6. We focus our analysis on the effects of observational biases on the measurements of the properties of ultra faint objects (UFOs, see Fig. 1).

To investigate whether UFOs are part of the (ultra-faint) DGs population, the GCs population or both; we first estimate the total number of FSCs based on a simple GC population synthesis model. This model assumes an initial distributions of star cluster masses and Galactocentric distances, which is then evolved by a simple mass loss prescription. We

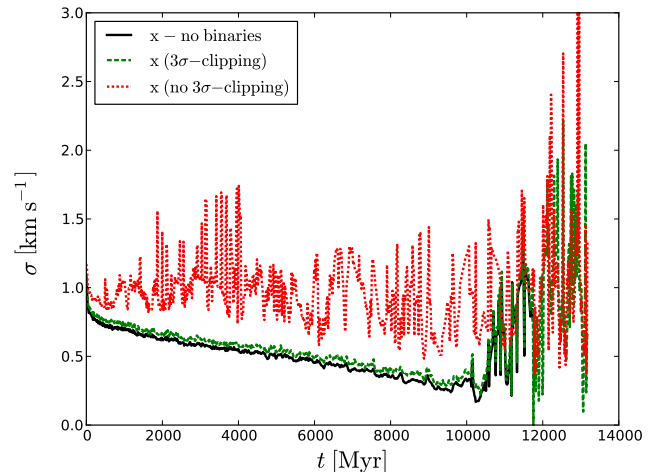


Figure 17. Evolution of the velocity dispersion along the x -axis for the model 50e50L-B2-BH including all the binaries (dotted red line), applying the 3σ -clipping technique (dashed green line), and without binaries (black line).

find that the predicted number of clusters ($N_{\text{FSC}} = 3.3^{+7.3}_{-1.6}$) is consistent with the number of observed star cluster candidates, see Fig. 2. However, more star clusters could be discovered and because we are using a very simple model, that for example ignores M/L_V variations, we cannot conclude that part of the UFOs are DGs.

Using a series of N -body simulations we further study the biases that may arise from observing FSCs. These simulations were projected along different lines-of-sight and the object properties were derived using traditional state-of-the-art methods ([Martin et al. 2008](#)). In order to investigate the role of the MW fore/background stars contamination we adopt a TRILEGAL-simulated field population at the position of two known UFOs (Koposov 1 and Willman 1). We find that the projected density of MW background stars can influence the measured size of a UFO in the sense that denser environments will lead to smaller sizes, when the Plummer model is not able to fit the number density profile properly (i.e. near apocentre and along the orbit, see Fig. 6).

Besides the effect of the projected density of MW field stars, we notice that the observed size of a UFO depends on the orbital phase. Objects closer to apocentre tend to appear larger, however this effect is highly dependent on the viewing angle of the simulations, since the apparent larger size is caused by the overlapping of tidal tail stars. We find that the size enhancement is visible when the object is observed along the y -axis (the cluster is orbiting on the x - y plane with positive angular momentum and the x -axis is the line that connect the Galactic centre to the cluster centre), for a small fraction of the orbit ($\sim 8\%$, for the model 50e50H).

The simulations also reveal a clear relation between cluster size and initial density in the sense that initially low-density clusters are more susceptible to size variations due to orbital phase (in all lines-of-sight). This result suggests that extended UFOs (eUFOs) are more likely to be observed if they formed Roche volume-filling. Furthermore, we observe that simulated clusters with pericentre roughly within the potential scale radius (R_0) show variations in the size

measurements. This appear to be due to the change of the NFW density slope near the scale radius, which ultimately influences the strength of the tidal forces.

From our analysis we conclude that compact UFO satellites (e.g. Kuposov 1 and 2) may naturally arise from a population of collisional systems. However, it is very unlikely that star clusters, that do not initially retain stellar mass BHs, contribute to the eUFO population of a MW-like galaxy. The probability of observing an eUFO becomes insignificant if we consider that it has to be viewed along the y -axis (the least probable line-of-sight) and near apocentre. Nevertheless, if a cluster forms filling its Roche volume and has its pericentre within the scale radius, the probability to observe it rise up to 30%. It means that among the FSC population, 1 over 3 could be observed extended. We find that these results hold even on multi-component (P90) or growing Galactic potential.

We find that the retention of stellar mass BHs (no natal kicks) radically changes the results. When the cluster is initially Roche-filling, the observed size (as the 3-D half-mass radius) is expanding for its entire lifetime. In particular, after 9 Gyr the observed size grows above 20 pc, independent of the line-of-sight and the fore/background. Whereas, when the cluster has an initial high density and retain 100% of BHs, the BHs do not change the evolution of the size because they are rapidly ejected due to two-body interaction. This scenario is partially supported by observations of stellar mass BHs in several GCs (Strader et al. 2012; Chomiuk et al. 2013). Moreover, indirect evidence for BH in GCs comes from the large core radii (Merritt et al. 2004; Mackey et al. 2007, 2008) and the absence of mass segregation in NGC6101 (Peuten et al. 2016).

Finally, we study the effect of primordial binaries in our simulations, in particular their effect on the velocity dispersion. If we combine the size and the velocity dispersion measurements from the simulations with stellar mass BHs and primordial binaries, we estimate a $M/L_V \sim 1 - 100$. High M/L_V values ($M/L_V \gtrsim 10$) are observed in DGs (McConnachie 2012), which are DM dominated objects, but our simulations show that these measurements are not conclusive for a DGs interpretation. We show that the binaries can inflate the velocity dispersion and that in an extended star cluster the properties of the binaries do not change significantly. Therefore, binaries with different initial properties may inflate the velocity dispersion and M/L_V even more. For this reason, because the initial properties of the binary population is unknown we have to rely on assumptions which may not be correct. However, Peñarrubia et al. (2016) show that wide binaries can be used to constrain the central distribution of DM in ultra-faint DGs. In addition to that, in some of the eUFOs, metallicity spread has been observed, which is indicative of an extended star formation history. This leads to the conclusion that the satellite is either a tidally disrupted DM-free galaxy, or a DG.

DGs have lower or similar metallicities than GCs but they also have a relaxation time longer than the Hubble time, which means that the dynamical evolution due to two-body relaxation is not important. Therefore, they have a mass function (MF) which is not depleted in low-mass stars as a result of dynamical evolution. However, Geha et al. (2013) showed that the MF of DGs becomes flatter with decreasing metallicity, which they attribute to IMF variations.

In GCs, mass segregation and evaporation can change the slope of the MF during the evolution (Vesperini & Heggie 1997; Baumgardt & Makino 2003), hence we expect GCs to be depleted in low-mass stars near the end of their lives, and to have a flatter MF for smaller Galactocentric distance.

eUFOs are likely to be accreted objects from DGs interacting with the MW, because if they form in a DG, the probability to be initially Roche-filling (low density) is enhanced (e.g. Elmegreen 2008). Therefore, if they form with a low density they have a large initial half-mass relaxation time and only few BHs will be expelled due to dynamical interactions. Moreover, an initially DM-dominated object will be likely to retain a high number of BHs even when natal kicks are taken into account. The BHs will sit in the centre pushing out the low mass particles due to two-body relaxation. Then, when the dissolution of the system occurs with few hundreds of stars left, a faint DM-free object can be observed.

Our results to some extent agree with Dominguez et al. (2016) results, where they claim that Segue 1, an eUFO, can be a DM-free object. Unfortunately, it is not trivial to compare our results with their results, because we are using a direct N -body code, ideal for collisional systems, while they are using a particle-mesh code, which is not ideal to simulate star clusters but less time consuming, as they stated in their conclusion. Therefore, they do not have stars with different masses and binaries stars, which in our cases are fundamental to increase the observed velocity dispersion. However, our simulations are not fine tuned for Segue 1.

In this paper, we conclude that star clusters contribute to both the compact and the extended population of UFOs. Retaining stellar mass BHs in an initially low density cluster is vital to have extended star cluster. While a high binary fraction can inflate the velocity dispersion measurements significantly, leading to the conclusion that the object has a high M/L_V ratio. It is possible to say something about the nature of star clusters that appear as an eUFO by considering the kinematics of the (tidal) tails, because in the case of dissolving star clusters these should be cold (few 100 m s^{-1}). Therefore, if the UFO is a star cluster we expect to observe a flatter MF for smaller Galactocentric distance and uncorrelated with metallicity, and dynamically cold tails; while mass segregation and binary properties cannot be used to discern between DM free and DM dominated object.

ACKNOWLEDGMENTS

MG acknowledges financial support from the Royal Society in the form of a University Research Fellowship (URF) and an equipment grant used for the GPU cluster in Surrey. All authors acknowledge support from the European Research Council (ERC-StG-335936, CLUSTERS). The authors thank Oscar Agertz, Florent Renaud, Alice Zocchi, Vincent Hénault-Brunet, Justin I. Read, Alessia Gualandris for interesting discussions and the referee for comments and suggestions. We are grateful to Sverre Aarseth and Keigo Nitadori for making NBODY6 publicly available, and to Dan Foreman-Mackey for providing the EMCEE software and for maintaining the online documentation; we also thank Mr David Munro of the University of Surrey for hardware and software support. The analyses done for this paper made

use of SCIPY (Jones et al. 2001), NUMPY (van der Walt et al. 2011), and MATPLOTLIB (Hunter 2007).

References

- Aarseth S. J., 2003, *Gravitational N-Body Simulations*. Cambridge University Press, November 2003.
- Abbott B. P., et al., 2016, *ApJ*, **818**, L22
- Ackermann M., et al., 2014, *Phys. Rev. D*, **89**, 042001
- Alexander P. E. R., Gieles M., 2012, *MNRAS*, **422**, 3415
- Alexander P. E. R., Gieles M., Lamers H. J. G. L. M., Baumgardt H., 2014, *MNRAS*, **442**, 1265
- Balbinot E., et al., 2013, *ApJ*, **767**, 101
- Baumgardt H., 2001, *MNRAS*, **325**, 1323
- Baumgardt H., Makino J., 2003, *MNRAS*, **340**, 227
- Baumgardt H., Mieske S., 2008, *MNRAS*, **391**, 942
- Bechtol K., Drlica-Wagner A., Balbinot E., Pieres A., Simon J. D., Yanny B., Santiago B., The DES Collaboration 2015, *ApJ*, **807**, 50
- Belokurov V., 2013, *New Astron. Rev.*, **57**, 100
- Belokurov V., et al., 2007, *ApJ*, **654**, 897
- Belokurov V., Irwin M. J., Koposov S. E., Evans N. W., Gonzalez-Solares E., Metcalfe N., Shanks T., 2014, *MNRAS*, **441**, 2124
- Breen P. G., Heggie D. C., 2013a, *MNRAS*, **432**, 2779
- Breen P. G., Heggie D. C., 2013b, *MNRAS*, **436**, 584
- Bressan A., Marigo P., Girardi L., Salasnich B., Dal Cero C., Rubele S., Nanni A., 2012, *MNRAS*, **427**, 127
- Buist H. J. T., Helmi A., 2014, *A&A*, **563**, A110
- Butler D., Dickens R. J., Epps E., 1978, *ApJ*, **225**, 148
- Cai M. X., Gieles M., Heggie D. C., Varri A. L., 2016, *MNRAS*, **455**, 596
- Cardelli J. A., Clayton G. C., Mathis J. S., 1989, *ApJ*, **345**, 245
- Cen R., Miralda-Escudé J., Ostriker J. P., Rauch M., 1994, *ApJ*, **437**, L9
- Chen Y., Girardi L., Bressan A., Marigo P., Barbieri M., Kong X., 2014, *MNRAS*, **444**, 2525
- Chomiuk L., Strader J., Maccarone T. J., Miller-Jones J. C. A., Heinke C., Noyola E., Seth A. C., Ransom S., 2013, *ApJ*, **777**, 69
- Cottaar M., Hénault-Brunet V., 2014, *A&A*, **562**, A20
- Davis M., Efstathiou G., Frenk C. S., White S. D. M., 1985, *ApJ*, **292**, 371
- De Marchi G., Paresce F., Portegies Zwart S., 2010, *ApJ*, **718**, 105
- Dickens R. J., Woolley R. v. d. R., 1967, *Royal Greenwich Observatory Bulletins*, **128**, 255
- Dominguez R., Fellhauer M., Blańa M., Farias J.-P., Dabringhausen J., Candlish G. N., Smith R., Choque N., 2016, preprint, ([arXiv:1606.08778](https://arxiv.org/abs/1606.08778))
- Drlica-Wagner A., et al., 2015a, *ApJ*, **809**, L4
- Drlica-Wagner A., Bechtol K., Rykoff E. S., Luque E., Queiroz A., Mao Y.-Y., Wechsler R. H., DES Collaboration 2015b, *ApJ*, **813**, 109
- Drlica-Wagner A., et al., 2016, preprint, ([arXiv:1609.02148](https://arxiv.org/abs/1609.02148))
- Elmegreen B. G., 2008, *ApJ*, **672**, 1006
- Fadely R., Willman B., Geha M., Walsh S., Muñoz R. R., Jerjen H., Vargas L. C., Da Costa G. S., 2011, *AJ*, **142**, 88
- Fall S. M., Zhang Q., 2001, *ApJ*, **561**, 751
- Foreman-Mackey D., Hogg D. W., Lang D., Goodman J., 2013, *PASP*, **125**, 306
- Freeman K. C., Rodgers A. W., 1975, *ApJ*, **201**, L71
- Fryer C. L., Belczynski K., Wiktorowicz G., Dominik M., Kalogera V., Holz D. E., 2012, *ApJ*, **749**, 91
- Geha M., et al., 2013, *ApJ*, **771**, 29
- Geringer-Sameth A., Walker M. G., Koushiappas S. M., Koposov S. E., Belokurov V., Torrealba G., Evans N. W., 2015, *Physical Review Letters*, **115**, 081101
- Gieles M., 2009, *MNRAS*, **394**, 2113
- Gieles M., Larsen S. S., Bastian N., Stein I. T., 2006, *A&A*, **450**, 129
- Gieles M., Heggie D. C., Zhao H., 2011, *MNRAS*, **413**, 2509
- Giersz M., Heggie D. C., 1997, *MNRAS*, **286**, 709
- Giersz M., Heggie D. C., 2011, *MNRAS*, **410**, 2698
- Gilmore G., Wilkinson M. I., Wyse R. F. G., Klyna J. T., Koch A., Evans N. W., Grebel E. K., 2007, *ApJ*, **663**, 948
- Girardi L., et al., 2012, TRILEGAL, a TRIdimensional modeL of the GALaxy: Status and Future. p. 165, [doi:10.1007/978-3-642-18418-5_17](https://doi.org/10.1007/978-3-642-18418-5_17)
- Goldsbury R., et al., 2012, *ApJ*, **760**, 78
- Gratton R., Sneden C., Carretta E., 2004, *ARA&A*, **42**, 385
- Harris W. E., 2010, [arXiv:1012.3224](https://arxiv.org/abs/1012.3224),
- Heggie D., Hut P., 2003, *The Gravitational Million-Body Problem: A Multidisciplinary Approach to Star Cluster Dynamics*. Cambridge University Press, 2003, 372 pp.
- Helmi A., White S. D. M., Springel V., 2003, *MNRAS*, **339**, 834
- Hénon M., 1961, *Annales d'Astrophysique*, **24**, 369; [English translation: ArXiv:1103.3499 \(H61\)](https://arxiv.org/abs/1103.3499)
- Heyl J., Richer H. B., Antolini E., Goldsbury R., Kalirai J., Parada J., Tremblay P.-E., 2015, *ApJ*, **804**, 53
- Hunter J. D., 2007, *Matplotlib: A 2D Graphics Environment*, [doi:10.1109/MCSE.2007.55](https://doi.org/10.1109/MCSE.2007.55), <http://matplotlib.org/>
- Hurley J. R., 2007, *MNRAS*, **379**, 93
- Hurley J. R., Pols O. R., Tout C. A., 2000, *MNRAS*, **315**, 543
- Hurley J. R., Tout C. A., Pols O. R., 2002, *MNRAS*, **329**, 897
- Hurley J. R., Aarseth S. J., Shara M. M., 2007, *ApJ*, **665**, 707
- Ivanova N., Belczynski K., Fregeau J. M., Rasio F. A., 2005, *MNRAS*, **358**, 572
- Jones E., Oliphant T., Peterson P., et al., 2001, *SciPy: Open source scientific tools for Python*, <http://www.scipy.org/>
- Jordán A., et al., 2007, *ApJS*, **171**, 101
- Kim D., Jerjen H., 2015, *ApJ*, **799**, 73
- Kim D., Jerjen H., Milone A. P., Mackey D., Da Costa G. S., 2015a, *ApJ*, **803**, 63
- Kim D., Jerjen H., Mackey D., Da Costa G. S., Milone A. P., 2015b, *ApJ*, **804**, L44
- Kim D., Jerjen H., Mackey D., Da Costa G. S., Milone A. P., 2016, *ApJ*, **820**, 119
- King I., 1962, *AJ*, **67**, 471
- Koposov S., et al., 2007, *ApJ*, **669**, 337
- Koposov S. E., Belokurov V., Torrealba G., Evans N. W., 2015, *ApJ*, **805**, 130
- Kroupa P., 1995, *MNRAS*, **277**, 1507
- Kroupa P., 1997, *New Astron.*, **2**, 139
- Kroupa P., 2001, *MNRAS*, **322**, 231
- Lada C. J., 2006, *ApJ*, **640**, L63
- Laevens B. P. M., et al., 2014, *ApJ*, **786**, L3
- Laevens B. P. M., et al., 2015a, *ApJ*, **802**, L18
- Laevens B. P. M., et al., 2015b, *ApJ*, **813**, 44
- Lamers H. J. G. L. M., Gieles M., Bastian N., Baumgardt H., Kharchenko N. V., Portegies Zwart S., 2005, *A&A*, **441**, 117
- Larsen S. S., 2009, *A&A*, **494**, 539
- Luque E., et al., 2015, preprint, ([arXiv:1508.02381](https://arxiv.org/abs/1508.02381))
- Lützgendorf N., Baumgardt H., Kruijssen J. M. D., 2013, *A&A*, **558**, A117
- Mackey A. D., Wilkinson M. I., Davies M. B., Gilmore G. F., 2007, *MNRAS*, **379**, L40
- Mackey A. D., Wilkinson M. I., Davies M. B., Gilmore G. F., 2008, *MNRAS*, **386**, 65
- Majewski S. R., 1993, *ARA&A*, **31**, 757
- Martin N. F., de Jong J. T. A., Rix H.-W., 2008, *ApJ*, **684**, 1075
- Martin N. F., et al., 2015, *ApJ*, **804**, L5
- Martin N. F., et al., 2016, *MNRAS*, **458**, L59
- Martinez G. D., Minor Q. E., Bullock J., Kaplinghat M., Simon J. D., Geha M., 2011, *ApJ*, **738**, 55
- Mashchenko S., Sills A., 2005a, *ApJ*, **619**, 243

Mashchenko S., Sills A., 2005b, *ApJ*, **619**, 258

Mateo M., 1997, in Arnaboldi M., Da Costa G. S., Saha P., eds, *Astronomical Society of the Pacific Conference Series Vol. 116, The Nature of Elliptical Galaxies; 2nd Stromlo Symposium*. p. 259 ([arXiv:astro-ph/9701158](https://arxiv.org/abs/astro-ph/9701158))

Mateo M. L., 1998, *ARA&A*, **36**, 435

McConnachie A. W., 2012, *AJ*, **144**, 4

McLaughlin D. E., van der Marel R. P., 2005, *ApJS*, **161**, 304

Merritt D., Piatek S., Portegies Zwart S., Hemsendorf M., 2004, *ApJ*, **608**, L25

Moore B., 1996, *ApJ*, **461**, L13

Muñoz R. R., Padmanabhan N., Geha M., 2012a, *ApJ*, **745**, 127

Muñoz R. R., Geha M., Côté P., Vargas L. C., Santana F. A., Stetson P., Simon J. D., Djorgovski S. G., 2012b, *ApJ*, **753**, L15

Navarro J. F., Frenk C. S., White S. D. M., 1996, *ApJ*, **462**, 563

Nelder J. A., Mead R., 1965, *The Computer Journal*, **7**, 308

Nitadori K., Aarseth S. J., 2012, *MNRAS*, **424**, 545

O'Donnell J. E., 1994, *ApJ*, **422**, 158

Olzewski E. W., 1998, in Zaritsky D., ed., *Astronomical Society of the Pacific Conference Series Vol. 136, Galactic Halos*. p. 70

Paczynski B., 1990, *ApJ*, **348**, 485

Paust N., Wilson D., van Belle G., 2014, *AJ*, **148**, 19

Peñarrubia J., Ludlow A. D., Chanamé J., Walker M. G., 2016, *MNRAS*, **461**, L72

Peuten M., Zocchi A., Gieles M., Gualandris A., Hénault-Brunet V., 2016, *MNRAS*, **462**, 2333

Plummer H. C., 1911, *MNRAS*, **71**, 460

Pryor C., Meylan G., 1993, in Djorgovski S. G., Meylan G., eds, *Astronomical Society of the Pacific Conference Series Vol. 50, Structure and Dynamics of Globular Clusters*. p. 357

Read J. I., 2014, *Journal of Physics G Nuclear Physics*, **41**, 063101

Renaud F., Gieles M., 2015a, preprint, ([arXiv:1503.04815](https://arxiv.org/abs/1503.04815))

Renaud F., Gieles M., 2015b, *MNRAS*, **448**, 3416

Renaud F., Gieles M., Boily C. M., 2011, *MNRAS*, **418**, 759

Repetto S., Davies M. B., Sigurdsson S., 2012, *MNRAS*, **425**, 2799

Sarajedini A., Layden A. C., 1995, *AJ*, **109**, 1086

Schechter P., 1976, *ApJ*, **203**, 297

Schlegel D. J., Finkbeiner D. P., Davis M., 1998, *ApJ*, **500**, 525

Shanahan R. L., Gieles M., 2015, *MNRAS*, **448**, L94

Simon J. D., et al., 2011, *ApJ*, **733**, 46

Springel V., Frenk C. S., White S. D. M., 2006, *Nature*, **440**, 1137

Strader J., Chomiuk L., Maccarone T. J., Miller-Jones J. C. A., Seth A. C., 2012, *Nature*, **490**, 71

Tang J., Bressan A., Rosenfield P., Slemmer A., Marigo P., Girardi L., Bianchi L., 2014, *MNRAS*, **445**, 4287

Tolstoy E., Hill V., Tosi M., 2009, *ARA&A*, **47**, 371

Torreallba G., Koposov S. E., Belokurov V., Irwin M., 2016a, *MNRAS*, **459**, 2370

Torreallba G., et al., 2016b, *MNRAS*, **463**, 712

Vesperini E., Heggie D. C., 1997, *MNRAS*, **289**, 898

Walker M., 2013, *Dark Matter in the Galactic Dwarf Spheroidal Satellites*. p. 1039, [doi:10.1007/978-94-007-5612-0_20](https://doi.org/10.1007/978-94-007-5612-0_20)

Walker M. G., Mateo M., Olszewski E. W., Peñarrubia J., Wyn Evans N., Gilmore G., 2009, *ApJ*, **704**, 1274

Wang J., et al., 2011, *MNRAS*, **413**, 1373

White S. D. M., Frenk C. S., Davis M., Efstathiou G., 1987, *ApJ*, **313**, 505

Willman B., Strader J., 2012, *AJ*, **144**, 76

Willman B., Blanton M. R., West A. A., Dalcanton J. J., Hogg D. W., Schneider D. P., Wherry N., et al. 2005, *AJ*, **129**, 2692

Willman B., et al., 2006, *ArXiv Astrophysics e-prints*,

Willman B., Geha M., Strader J., Strigari L. E., Simon J. D., Kirby E., Ho N., Warren A., 2011, *AJ*, **142**, 128

Wolf J., Martinez G. D., Bullock J. S., Kaplinghat M., Geha M., Muñoz R. R., Simon J. D., Avedo F. F., 2010, *MNRAS*, **406**, 1220

Yahil A., Vidal N. V., 1977, *ApJ*, **214**, 347

York D. G., et al., 2000, *AJ*, **120**, 1579

van den Bosch F. C., Lewis G. F., Lake G., Stadel J., 1999, *ApJ*, **515**, 50

van der Walt S., Colbert C. S., Varoquaux G., 2011, *The NumPy Array: A Structure for Efficient Numerical Computation*, [doi:10.1109/MCSE.2011.37](https://doi.org/10.1109/MCSE.2011.37), <http://www.numpy.org/>

APPENDIX A: ABSOLUTE MAGNITUDE IN V-BAND

To compute the V -band absolute magnitude (M_V) of the simulated clusters we applied two methods.

1) Knowing the luminosity (L in L_\odot) and the temperature (T in K) of each star (NBODY6 output) is possible to calculate M_V .

$$M_V = -2.5 \log \sum_{i=1}^N 10^{-0.4M_{V_i}} \quad (\text{A1})$$

here M_{V_i} is the absolute magnitude in band V of the i -th star and N is the total number of stars.

$$M_{V_i} = M_{V,\odot} - 2.5 \log \left(\frac{L_i}{L_\odot} \right) - \text{BC} \quad (\text{A2})$$

where $M_{V,\odot} = 4.8$ is the absolute magnitude of the Sun and BC is the bolometric correction:

$$\text{BC} = 2.324497 + 2.5 \log(g(T_i)) \quad (\text{A3})$$

with

$$g(T_i) = BB(\lambda, T_i) \cdot \Delta_\lambda \quad (\text{A4})$$

where $\Delta_\lambda = 88 \cdot 10^{-9}$ m is the full width at half maximum (FWHM) of V -band filter. While $BB(\lambda, T_i)$ is the normalised black body radiation formula (Planck law):

$$BB(\lambda, T_i) = \frac{1}{BB_{tot}(T_i)} \frac{BB_0(\lambda)}{e^{\frac{hc}{\lambda K_B T_i}} - 1} \quad (\text{A5})$$

with $BB_0 = \frac{2hc^2}{\lambda^5}$ and $BB_{tot} = \frac{\sigma}{\pi} T_i^4$. Where c is the speed of light, h is the Planck constant, σ is the Stefan-Boltzmann constant, K_B is the Boltzmann constant. In our case we use $\lambda = 551$ nm, which is the central wavelength for the V -band filter.

2) We compute the absolute magnitude in band V using the initial mass of the stars in the simulations.

From eq. (A1) we need to compute M_{V_i} . Using CMD 2.7, we can use the PARSEC isochrones v1.2S (Bressan et al. 2012; Chen et al. 2014; Tang et al. 2014), where the initial mass (m_i^{model}) of the stars and their absolute magnitude in V -band ($M_{V_i}^{model}$) are given for a selected time.

At this point, we can generate a function which interpolate these data, therefore, we have the absolute magnitude in V -band as a function of the initial mass, $M_{V_i}^{model}(m_i^{model})$. Using the initial mass of the surviving stars at fixed time in our simulations, we can estimate their absolute magnitude in V -band, $M_{V_i}^{model}(m_i^{N-body})$.

In conclusion the two methods are equivalent because we obtain similar results.